

Thermal freeze-out parameters and pseudo-entropy from charged hadron spectra in high energy collisions

Xu-Hong Zhang^{1,*}, Ya-Qin Gao^{2,†}, Fu-Hu Liu^{1,‡}, Khusniddin K. Olimov^{3,§}

¹*Institute of Theoretical Physics, State Key Laboratory of Quantum Optics and Quantum Optics Devices
& Collaborative Innovation Center of Extreme Optics, Shanxi University, Taiyuan 030006, China*

²*Department of Physics, Taiyuan University of Science and Technology, Taiyuan 030024, China*

³*Laboratory of High Energy Physics, Physical-Technical Institute of Uzbekistan Academy of Sciences,
Chingiz Aytmatov str. 2^b, 100084 Tashkent, Uzbekistan*

Abstract: We collected the transverse momentum (mass) spectra of charged hadrons (π^- , π^+ , K^- , K^+ , \bar{p} , and p) produced in collisions over a center-of-mass energy range from 2.70 to 200 GeV (per nucleon pair). The modified Tsallis–Pareto-type function (the TP-like function) with average transverse flow velocity is used to describe the contribution of participant or constituent quarks to transverse momentum of considered hadron. The experimental spectra of π^\mp and K^\mp (or \bar{p} and p) are fitted by the convolution of two (or three) TP-like functions due to the fact that two (or three) constituent quarks are regarded as two (or three) energy resources in the formation of considered hadron. From the reasonable fits to the spectra, the thermal freeze-out parameters are extracted, and the pseudo-entropy is newly defined and extracted. Some parameters quickly change in the energy range of less than 7.7 GeV, and slowly change in the energy range of greater than 7.7 GeV, indicating the variation of collision mechanism at around 7.7 GeV.

Keywords: Thermal freeze-out parameters, pseudo-entropy, charged hadron spectra, relativistic Au-Au collisions

PACS: 12.40.Ee, 13.85.Hd, 24.10.Pa

I. INTRODUCTION

As the basic gauge field theory [1–3] which is used for describing strong interactions, Quantum Chromodynamics (QCD) predicts that under the condition of high temperature and high density [4], partons can be released from the confined hadron phase to form a new form of substance that is called Quark-Gluon Plasma (QGP) [5–8]. The high-temperature and high-density fireball formed in relativistic heavy-ion collisions can take the shape of this kind of new form of strongly interacting substance. In the meantime, the particular system com-

posed by this kind of substance is usually described by the QCD phase diagram [9, 10]. Nevertheless, once the external conditions are changed, the strongly interacting substances described by QCD will undergo a phase transition [9, 10]. On the one hand, if the thermodynamic properties of the system are expressed by the temperature and the chemical potential of baryons [11–13], the first-order phase transition will occur in the region where the chemical potential of baryons is higher and the temperature is lower. On the other hand, in the region where both the baryon chemical potential [11–13] and temperature are high, the system maintains dynamic balance which passes a smooth transition. In other words, there is a critical point [14–19] from hadronic to QGP phases in the deconfinement process, that is the end point of the first-order phase transition of the QCD matter.

One of the most important targets of relativistic

*xhzhang618@163.com; zhang-xuhong@qq.com

†gyq610@163.com; gaoyaqin@tyust.edu.cn

‡Correspondence: fuhuliu@163.com; fuhuliu@sxu.edu.cn

§Correspondence: khkolimov@gmail.com; kh.olimov@uzsci.net

heavy-ion collisions [20–23] is to explore the QCD phase diagram, understand the structure of QGP, and determine the phase boundary [24, 25] between different phases. The Beam Energy Scan (BES) project [26–29] started by the Relativistic Heavy Ion Collider (RHIC) in 2010 is to study the phase diagram [9, 10] of strongly interacting nuclear matter. The RHIC-BES program [30–32] is performed for mainly three objectives: The first one is to find the onset energy of deconfinement phase transition [9, 10]. The second one is to identify the critical point of the QCD phase diagram [9, 10, 14–17]. And the third one is to determine the characteristics of the first-order phase transition. Since the baryon chemical potential of matter is related to the collision energy [11–13], researchers expect to find the corresponding critical point of phase transition by the way of changing the collision energy. The RHIC-BES program including its fixed target experiments is able to vary the collision energy over a wide range in low energy region, thereby achieving an extensive range of baryon chemical potential, further expanding the search objective.

Hadrons are particles involved in strong interactions, including two kinds of particles: mesons (bosons) and baryons (fermions). The most common mesons measured in experiments include, but are not limited to, negatively and positively charged π mesons (π^- and π^+), negatively and positively charged K mesons (K^- and K^+), etc. The most common baryons measured in experiments include, but are not limited to, anti-protons and protons (\bar{p} and p), etc. In the RHIC-BES program and at the previous and lower energy such as the Alternating Gradient Synchrotron (AGS) energy, π^- , π^+ , K^- , K^+ , \bar{p} , and p are particularly important. In fact, the abundant transverse momentum (mass) spectra of the mentioned charged hadrons can be used to extract the common thermal parameters such as the freeze-out temperature and transverse flow velocity. Meanwhile, the novel pseudo-entropy, which will be defined later in this paper, can be also extracted from the spectra.

In this paper, the transverse momentum spectra of π^- , π^+ , K^- , K^+ , \bar{p} , and p produced at mid-rapidity (mid- y) in gold-gold (Au-Au) collisions with different centralities at the RHIC and its BES energy [33–35] are collected. Meanwhile, the transverse mass spectra of the mentioned charged hadrons produced at mid- y in central Au-Au collisions at the AGS energy [36–38] are also col-

lected, though the spectra of \bar{p} are not available due to low energy. These spectra are used to extract the thermal freeze-out parameters and the pseudo-entropy.

The remainder of this paper is structured as follows. The formalism and method are briefly introduced in Section 2. The results and discussion are given in Section 3. In Section 4, we summarize our main observations and conclusions.

II. FORMALISM AND METHOD

Non-extensive thermodynamics is a new method for studying heavy-ion collisions at relativistic energy. In the collisions such as in Au-Au collisions, the Tsallis–Pareto-type function [39–44] can fit the transverse momentum (p_T) spectra in low and intermediate regions, particularly in the final-state or hadronization process, demonstrating a strong relation among particles. However, in very low- p_T region, the fit result is not ideal, and the meaning of Tsallis parameters remains an open question.

In order to better fit the spectra in very low- p_T region, we express the information contained in the parameter more intuitively using the modified Tsallis–Pareto-type function (the TP-like function) as follows [45, 46]:

$$f_{p_T}(p_T) = \frac{1}{N} \frac{dN}{dp_T} = C p_T^{a_0} \left(1 + \frac{m_T - m_0}{nT} \right)^{-n}. \quad (1)$$

Here N is the number of particles, C is the normalization constant, m_0 is the rest mass of the considered particle, n is the power index that describes the degree of non-equilibrium, T is the effective temperature of the collision system, a_0 is the correction index, and $m_T = \sqrt{p_T^2 + m_0^2}$ is the transverse mass of the particle. As an extension, the TP-like function is naturally converged to the Tsallis–Pareto-type function if we set $a_0 = 1$ in Eq. (1).

In order to obtain the thermal or kinetic (or kinematic) freeze-out temperature T_0 and the average transverse flow velocity $\langle\beta_t\rangle$ [47, 48], one may fit firstly the p_T spectra of particles to obtain the effective temperature T . The average p_T ($\langle p_T \rangle$) and average energy (\overline{m}) of particles in the source rest frame can be obtained by using the Monte Carlo algorithm. Then, one may extract the intercept as T_0 in the linear relation of T versus m_0 , and further obtain the slope as $\langle\beta_t\rangle$ in the linear relation of $\langle p_T \rangle$ versus \overline{m} .

For purpose of simplifying this complicated solution

process, based on the idea of other work [49], we modify m_T and p_T in Eq. (1). For clarity, we use m'_T and p'_T instead of m_T and p_T in Eq. (1) respectively. The Lorentz-like transformation is $m'_T = \langle \gamma_t \rangle (m_T - p_T \langle \beta_t \rangle)$ and $|p'_T| = \langle \gamma_t \rangle |p_T - m_T \langle \beta_t \rangle|$, where $\langle \gamma_t \rangle = 1/\sqrt{1 - \langle \beta_t \rangle^2}$ is the Lorentz-like factor. The absolute value $|p_T - m_T \langle \beta_t \rangle|$ is used due to the fact that p'_T is positive and $p_T - m_T \langle \beta_t \rangle$ is possibly negative in low- p_T region. After the conversion, the new TP-like function $f(p_T)$ certainly obeys the relation $f_{p'_T}(p'_T)|dp'_T| = f(p_T)|dp_T|$. We have

$$f(p_T) = C \frac{\langle \gamma_t \rangle^{a_0+1}}{m_T} (m_T - p_T \langle \beta_t \rangle) |p_T - m_T \langle \beta_t \rangle|^{a_0} \times \left[1 + \frac{\langle \gamma_t \rangle (m_T - p_T \langle \beta_t \rangle) - m_0}{nT_0} \right]^{-n}. \quad (2)$$

One can see that T in Eq. (1) is naturally converted to T_0 in Eq. (2).

Our exploratory research shows that although Eq. (2) is applicable in the fit of p_T spectra, it is not flexible in some cases and explicable in depth at quark level due to m_0 being the rest mass of the considered particle. Empirically, Eq. (2) can be regarded as the probability density function obeyed by the transverse momentum p_{ti} of the i -th constituent quark that contributes to p_T of particle. Concretely, we have new TP-like function to be

$$f_i(p_{ti}) = C_i \frac{\langle \gamma_t \rangle^{a_0+1}}{m_{ti}} (m_{ti} - p_{ti} \langle \beta_t \rangle) |p_{ti} - m_{ti} \langle \beta_t \rangle|^{a_0} \times \left[1 + \frac{\langle \gamma_t \rangle (m_{ti} - p_{ti} \langle \beta_t \rangle) - m_{0i}}{nT_0} \right]^{-n}, \quad (3)$$

where m_{0i} is the constituent mass (0.31 MeV/ c^2 for u and d quarks and 0.5 GeV/ c^2 for s quark, as given in general textbook [50]) and $m_{ti} = \sqrt{p_{ti}^2 + m_{0i}^2}$ is the transverse mass of the i -th quark.

For a meson, $p_T = p_{t1} + p_{t2}$ due to two constituent quarks which contribute independently. The probability density function of meson's p_T is the convolution of two TP-like functions. For a baryon, $p_T = p_{t1} + p_{t2} + p_{t3}$ due to three constituent quarks which also contribute independently. The probability density function of baryon's p_T is the convolution of three TP-like functions. This analysis is at the quark level due to the fact that it is based on the constituent mass of quark. The present method is similar to the analysis at the particle level in terms of the similar convolution.

For mesons, we have the convolution of two TP-like functions to be

$$f(p_T) = \int_0^{p_T} f_1(p_{t1}) f_2(p_T - p_{t1}) dp_{t1} = \int_0^{p_T} f_2(p_{t2}) f_1(p_T - p_{t2}) dp_{t2}. \quad (4)$$

For baryons, we have the convolution of the first two TP-like functions to be

$$f_{12}(p_{t12}) = \int_0^{p_{t12}} f_1(p_{t1}) f_2(p_{t12} - p_{t1}) dp_{t1} = \int_0^{p_{t12}} f_2(p_{t2}) f_1(p_{t12} - p_{t2}) dp_{t2}. \quad (5)$$

The convolution of three TP-like functions is

$$f(p_T) = \int_0^{p_T} f_{12}(p_{t12}) f_3(p_T - p_{t12}) dp_{t12} = \int_0^{p_T} f_3(p_{t3}) f_{12}(p_T - p_{t3}) dp_{t3}. \quad (6)$$

In some cases, the spectra in experiments are for m_T . We need to convert the probability density function $[f(p_T)]$ of p_T to that $[f_{m_T}(m_T)]$ of m_T . In fact, we have the relation $f(p_T)|dp_T| = f_{m_T}(m_T)|dm_T|$. Further, we have

$$f_{m_T}(m_T) = \frac{m_T}{\sqrt{m_T^2 - m_0^2}} f\left(\sqrt{m_T^2 - m_0^2}\right). \quad (7)$$

For invariant p_T and m_T spectra which are used usually in experiments, we have

$$\frac{1}{2\pi p_T} \frac{d^2 N}{dp_T dy} = \frac{1}{2\pi m_T} \frac{d^2 N}{dm_T dy}. \quad (8)$$

Other forms of experimental spectra can be transformed from Eq. (8) conveniently if dy and the cross section are considered reasonably.

According to statistical physics and information theory, the essence of entropy is an expression of the degree of chaos existed inherently in a system [51–54]. Entropy has a certain relationship with the probability density function in thermodynamics. In order to further study the role of color confinement in relativistic heavy-ion collisions, the quantum entanglement entropy (the entropy of gluons or partons) is proposed to explore the underlying mechanism. As we know, the relationship between the measured particle multiplicity distribution in the deep inelastic scattering process and the entropy of final hadrons is expressed as [51–54]

$$S_{hadron} = - \sum P(N) \ln P(N), \quad (9)$$

where $P(N)$ is the multiplicity distribution of the charged particles measured in a given measurement area. The entropy of hadrons is assumed to be equal to the partonic entropy [51–54].

The TP-like function and the corresponding convolutions, which are used to describe the p_{ti} and p_T distributions respectively, are also the probability density functions. Analogous to the multiplicity distribution of the above formula, for the first time, we define the pseudo-entropy as follows:

$$S'_{hadron} = - \sum f(p_T) \ln f(p_T) \quad (10)$$

in which the p_T distribution $f(p_T)$ replaced the multiplicity distribution $P(N)$ in Eq. (9). Different from $P(N)$ in which N is discrete, p_T in $f(p_T)$ is continuous. To give a suitable and uniform description, we set the bin width of p_T to be 0.1 GeV/ c in the considered energy range in this paper. Although the pseudo-entropy is the bin width dependent, we may compare the relative sizes in different cases if the bin width is beforehand fixed.

III. RESULTS AND DISCUSSION

A. Comparison with data

Figure 1 shows the p_T spectra, $(1/2\pi p_T)d^2N/dp_T dy$, of π^- (a), π^+ (b), K^- (c), K^+ (d), \bar{p} (e), and p (f) produced at mid- y ($|y| < 0.1$) in Au-Au collisions at center-of-mass energy $\sqrt{s_{NN}} = 7.7$ GeV (per nucleon pair) with different centrality intervals. The symbols represent the experimental data measured by the STAR Collaboration in the RHIC-BES project [33, 34] and re-scaled by different amounts marked in the panels for clarity. The curves in Figures 1(a)–1(d) represent the results fitted by the convolution of two TP-like functions, for the spectra of π^\mp and K^\mp . The curves for the spectra of \bar{p} (e) and p (f) are the results fitted by the convolution of three TP-like functions. We have used the method of least squares to determine the values of parameters, and the method of statistical simulation to determine the errors of parameters. The values of n , T_0 , a_0 , $\langle\beta_t\rangle$, χ^2 , and degrees of freedom (ndof) are listed in Table 1. It can be seen that the convolution of two (three) TP-like functions fits well the experimental spectra of π^\mp and K^\mp (\bar{p} and p) produced in 7.7 GeV Au-Au collisions with different centrality intervals in the available p_T range.

Similarly, the p_T spectra of π^- (a), π^+ (b), K^- (c), K^+ (d), \bar{p} (e), and p (f) produced at mid- y in Au-Au collisions with different centrality intervals at $\sqrt{s_{NN}} = 11.5, 14.5, 19.6, 27,$ and 39 GeV are demonstrated in Figures 2–6, respectively, where the data are cited from the STAR Collaboration [33, 34]. The values of parameters, χ^2 , and ndof are listed in Tables 2–6 for different energies. One can see that the convolution of two (three) TP-like functions fits well the experimental spectra of π^\mp and K^\mp (\bar{p} and p) produced in Au-Au collisions at 11.5, 14.5, 19.6, 27, and 39 GeV with different centrality intervals in the available p_T range.

In order to better explore the change trends of parameters, besides the RHIC-BES energies, we have also conducted data collection and research on the p_T spectra at other RHIC energies. Figures 7–9 show the p_T spectra of π^- (a), π^+ (b), K^- (c), K^+ (d), \bar{p} (e), and p (f) produced in Au-Au collisions at 62.4, 130, and 200 GeV, respectively. The data with $|y| < 0.1$ are also cited from the STAR Collaboration [35]. The centrality intervals at 62.4 and 200 GeV are the same as those at RHIC-BES energies. However, the centrality intervals at 130 GeV are somehow different from others. The related parameters are listed in Tables 7–9 for different energies. One can see again that the convolution of two (three) TP-like functions fits well the experimental spectra of π^\mp and K^\mp (\bar{p} and p) produced in Au-Au collisions at 62.4, 130, and 200 GeV with different centrality intervals in the available p_T range.

Except the above comparisons, we have studied the m_T spectra of π^- (a), π^+ (b), K^- (c), K^+ (d), and p (e) produced at mid- y in 0–5% Au-Au collisions at $\sqrt{s_{NN}} = 2.70, 3.32, 3.84, 4.30,$ and 4.88 GeV in Figure 10, where the five energies are only available in panel (d). The symbols for π^\mp in $|y| < 0.05$, K^\mp in $|y| < 0.25$, and p in $|y| < 0.05$ represent the experimental data measured by the E895 [36], E866 [37], and E895 [38] Collaborations, respectively, where some sets of data are re-scaled by different amounts for clarity. The data for \bar{p} is not available in the same or similar experiments due to low energy. The related parameters are listed in Table 10. One can see that the convolution of two (three) TP-like functions fits approximately the experimental spectra of π^\mp and K^\mp (p) produced in 0–5% Au-Au collisions at 2.70, 3.32, 3.84, 4.30, and 4.88 GeV.

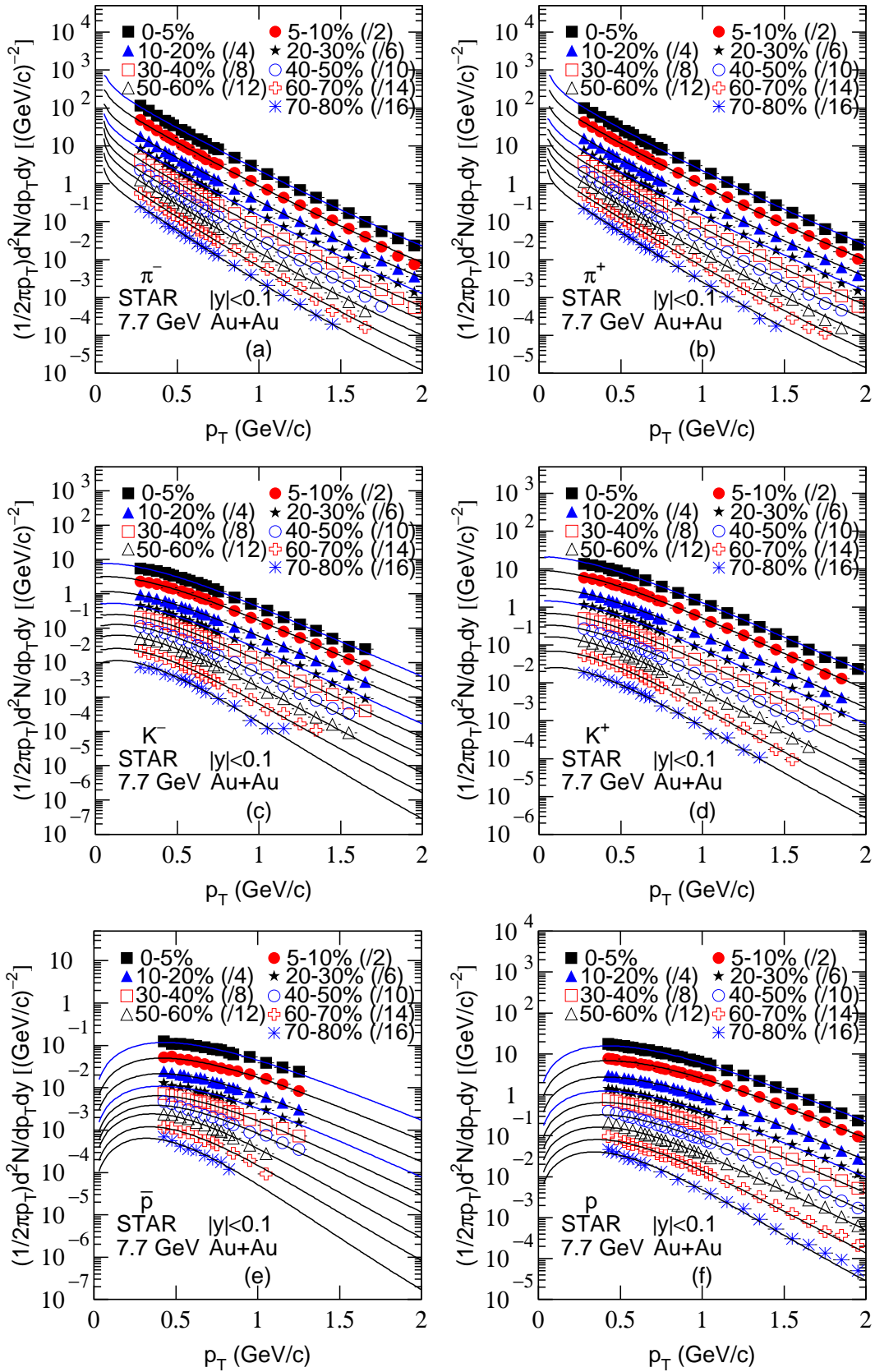


Figure 1. Transverse momentum spectra of π^- (a), π^+ (b), K^- (c), K^+ (d), \bar{p} (e), and p (f) produced in 7.7 GeV Au-Au collisions with various centrality intervals and at the mid-rapidity. The symbols represent the experimental data measured by the STAR Collaboration in the RHIC-BES program [33, 34] and re-scaled by different amounts marked in the panels. The curves are our results fitted by Eq. (4) for π^\pm and K^\pm [panels (a)–(d)] or Eq. (6) for \bar{p} and p [panels (e) and (f)].

Table 1. Values of n , T_0 , a_0 , $\langle\beta_t\rangle$, χ^2 , and ndof corresponding to the curves in Figure 1.

Figure	Particle	$\sqrt{s_{NN}}$ (GeV)	Selection	n	T_0 (GeV)	a_0	$\langle\beta_t\rangle$ (c)	χ^2/ndof	
Figure 1(a)	π^-	7.7	0–5%	17.8 ± 0.7	0.165 ± 0.003	-0.396 ± 0.005	0.112 ± 0.003	14/21	
			$ y < 0.1$	5–10%	16.5 ± 0.7	0.158 ± 0.003	-0.383 ± 0.005	0.109 ± 0.003	27/21
			10–20%	15.0 ± 0.5	0.155 ± 0.003	-0.379 ± 0.005	0.106 ± 0.003	8/21	
			20–30%	14.9 ± 0.5	0.150 ± 0.003	-0.374 ± 0.005	0.102 ± 0.003	14/21	
			30–40%	14.6 ± 0.5	0.147 ± 0.002	-0.369 ± 0.004	0.099 ± 0.002	18/21	
			40–50%	14.4 ± 0.5	0.143 ± 0.002	-0.365 ± 0.004	0.098 ± 0.002	15/19	
			50–60%	14.0 ± 0.4	0.135 ± 0.002	-0.362 ± 0.004	0.098 ± 0.002	10/18	
			60–70%	13.8 ± 0.4	0.128 ± 0.002	-0.358 ± 0.004	0.094 ± 0.002	17/18	
			70–80%	13.7 ± 0.4	0.121 ± 0.002	-0.356 ± 0.004	0.093 ± 0.002	6/16	
Figure 1(b)	π^+	7.7	0–5%	18.2 ± 0.8	0.171 ± 0.003	-0.420 ± 0.005	0.119 ± 0.003	12/21	
			$ y < 0.1$	5–10%	17.3 ± 0.7	0.168 ± 0.003	-0.417 ± 0.005	0.116 ± 0.003	5/21
			10–20%	16.0 ± 0.6	0.164 ± 0.003	-0.411 ± 0.005	0.114 ± 0.003	5/21	
			20–30%	15.7 ± 0.6	0.160 ± 0.003	-0.400 ± 0.005	0.111 ± 0.003	9/21	
			30–40%	15.3 ± 0.6	0.154 ± 0.003	-0.398 ± 0.005	0.109 ± 0.003	12/21	
			40–50%	14.9 ± 0.5	0.147 ± 0.002	-0.390 ± 0.005	0.106 ± 0.003	6/20	
			50–60%	14.4 ± 0.5	0.138 ± 0.002	-0.385 ± 0.005	0.104 ± 0.003	15/20	
			60–70%	13.9 ± 0.4	0.133 ± 0.002	-0.377 ± 0.005	0.102 ± 0.003	13/19	
			70–80%	13.4 ± 0.4	0.126 ± 0.002	-0.370 ± 0.005	0.100 ± 0.002	10/16	
Figure 1(c)	K^-	7.7	0–5%	27.9 ± 1.7	0.147 ± 0.002	0.011 ± 0.004	0.106 ± 0.005	9/18	
			$ y < 0.1$	5–10%	24.8 ± 1.4	0.143 ± 0.002	0.018 ± 0.004	0.105 ± 0.005	3/18
			10–20%	22.8 ± 1.2	0.139 ± 0.002	0.025 ± 0.004	0.103 ± 0.005	5/18	
			20–30%	21.8 ± 1.1	0.129 ± 0.002	0.045 ± 0.005	0.102 ± 0.005	8/18	
			30–40%	21.5 ± 1.1	0.124 ± 0.002	0.061 ± 0.005	0.101 ± 0.005	5/18	
			40–50%	20.8 ± 1.0	0.115 ± 0.002	0.070 ± 0.005	0.096 ± 0.004	11/15	
			50–60%	20.6 ± 1.0	0.107 ± 0.002	0.081 ± 0.005	0.096 ± 0.004	5/16	
			60–70%	18.9 ± 0.8	0.100 ± 0.002	0.085 ± 0.005	0.094 ± 0.004	11/14	
			70–80%	18.2 ± 0.8	0.089 ± 0.002	0.093 ± 0.005	0.092 ± 0.004	26/11	
Figure 1(d)	K^+	7.7	0–5%	29.1 ± 1.9	0.164 ± 0.003	-0.022 ± 0.004	0.124 ± 0.005	9/18	
			$ y < 0.1$	5–10%	27.2 ± 1.7	0.160 ± 0.003	-0.020 ± 0.004	0.112 ± 0.005	6/20
			10–20%	25.7 ± 1.5	0.155 ± 0.003	0.001 ± 0.004	0.109 ± 0.005	6/20	
			20–30%	25.1 ± 1.5	0.149 ± 0.002	0.005 ± 0.004	0.105 ± 0.005	5/20	
			30–40%	24.5 ± 1.4	0.144 ± 0.002	0.014 ± 0.004	0.099 ± 0.004	4/19	
			40–50%	22.5 ± 1.2	0.139 ± 0.002	0.019 ± 0.004	0.091 ± 0.004	9/18	
			50–60%	21.9 ± 1.1	0.129 ± 0.002	0.027 ± 0.004	0.085 ± 0.004	7/17	
			60–70%	20.1 ± 1.0	0.120 ± 0.002	0.034 ± 0.005	0.082 ± 0.004	8/16	
			70–80%	18.7 ± 0.8	0.112 ± 0.002	0.049 ± 0.005	0.079 ± 0.004	9/13	
Figure 1(e)	\bar{p}	7.7	0–5%	16.6 ± 0.7	0.128 ± 0.002	0.006 ± 0.004	0.347 ± 0.008	2/10	
			$ y < 0.1$	5–10%	15.8 ± 0.6	0.123 ± 0.002	0.007 ± 0.004	0.336 ± 0.008	4/9
			10–20%	15.1 ± 0.6	0.116 ± 0.002	0.011 ± 0.004	0.325 ± 0.008	5/13	
			20–30%	14.6 ± 0.5	0.113 ± 0.002	0.015 ± 0.004	0.317 ± 0.008	5/11	
			30–40%	13.6 ± 0.4	0.104 ± 0.002	0.017 ± 0.004	0.309 ± 0.008	6/12	
			40–50%	12.8 ± 0.3	0.098 ± 0.002	0.020 ± 0.004	0.291 ± 0.007	11/9	
			50–60%	12.5 ± 0.3	0.086 ± 0.001	0.020 ± 0.004	0.276 ± 0.007	1/8	
			60–70%	11.9 ± 0.3	0.079 ± 0.001	0.023 ± 0.004	0.271 ± 0.007	2/6	
			70–80%	11.2 ± 0.3	0.069 ± 0.001	0.024 ± 0.004	0.260 ± 0.007	2/4	
Figure 1(f)	p	7.7	0–5%	18.4 ± 0.8	0.129 ± 0.002	0.006 ± 0.004	0.346 ± 0.008	5/24	
			$ y < 0.1$	5–10%	17.6 ± 0.7	0.127 ± 0.002	0.011 ± 0.004	0.334 ± 0.008	4/24
			10–20%	16.7 ± 0.7	0.120 ± 0.002	0.016 ± 0.004	0.321 ± 0.008	4/24	
			20–30%	16.4 ± 0.7	0.117 ± 0.002	0.017 ± 0.004	0.314 ± 0.008	5/24	
			30–40%	15.0 ± 0.5	0.112 ± 0.002	0.019 ± 0.004	0.304 ± 0.008	9/23	
			40–50%	14.6 ± 0.5	0.105 ± 0.002	0.021 ± 0.004	0.298 ± 0.007	11/23	
			50–60%	13.4 ± 0.4	0.100 ± 0.002	0.023 ± 0.004	0.282 ± 0.007	16/22	
			60–70%	12.5 ± 0.3	0.091 ± 0.001	0.025 ± 0.004	0.271 ± 0.007	20/13	
			70–80%	11.2 ± 0.3	0.069 ± 0.001	0.024 ± 0.004	0.260 ± 0.007	2/4	

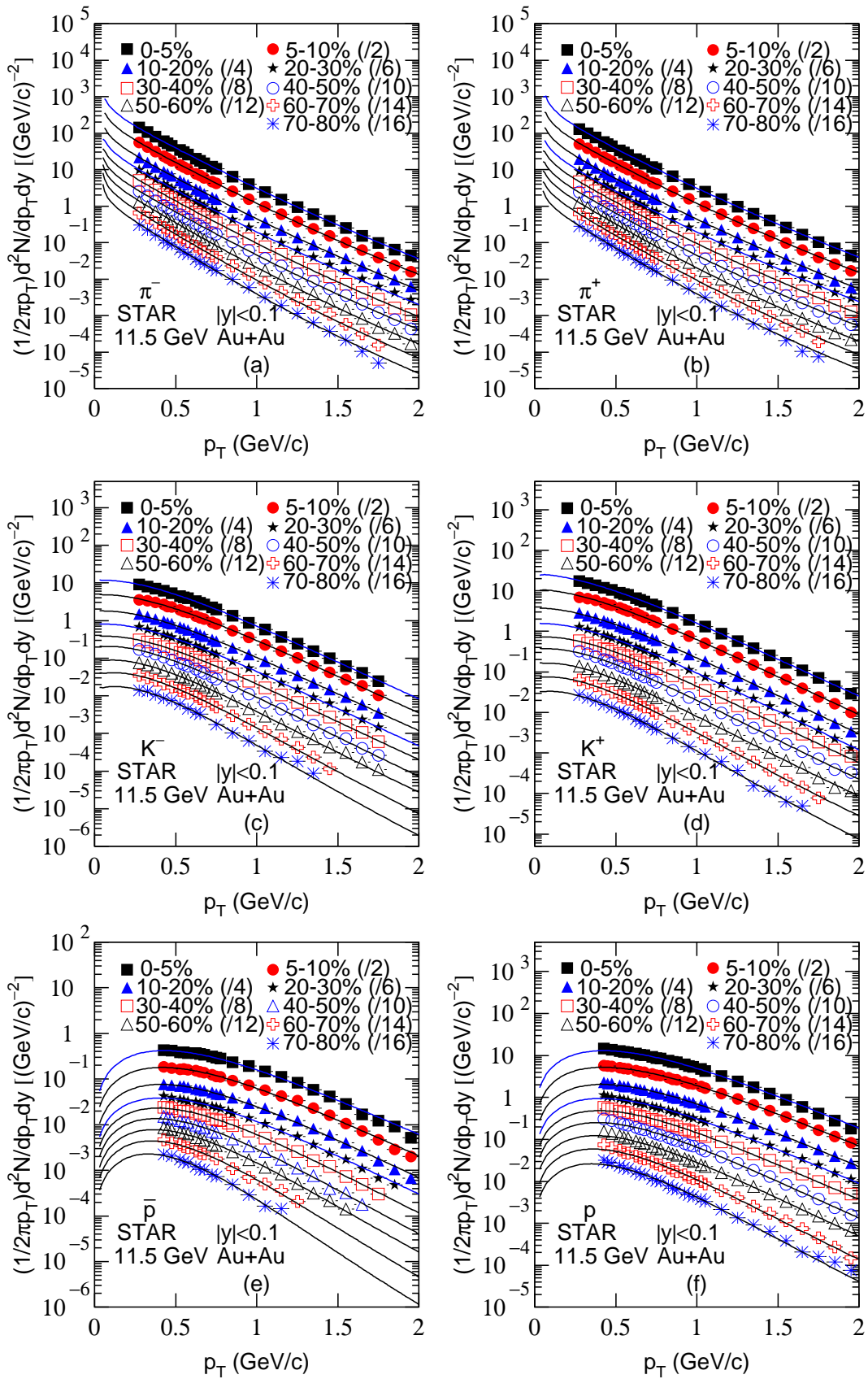


Figure 2. Same as Figure 1, but showing the results for 11.5 GeV Au-Au collisions. The symbols represent the STAR data [33].

Table 2. Values of n , T_0 , a_0 , $\langle\beta_t\rangle$, χ^2 , and ndof corresponding to the curves in Figure 2.

Figure	Particle	$\sqrt{s_{NN}}$ (GeV)	Selection	n	T_0 (GeV)	a_0	$\langle\beta_t\rangle$ (c)	χ^2/ndof	
Figure 2(a)	π^-	11.5	0-5%	16.0 ± 0.6	0.168 ± 0.003	-0.397 ± 0.005	0.114 ± 0.003	3/21	
			$ y < 0.1$	5-10%	14.5 ± 0.5	0.162 ± 0.003	-0.396 ± 0.005	0.113 ± 0.003	6/21
				10-20%	13.4 ± 0.4	0.158 ± 0.003	-0.389 ± 0.005	0.110 ± 0.003	6/21
				20-30%	13.4 ± 0.4	0.153 ± 0.003	-0.382 ± 0.005	0.109 ± 0.003	20/21
				30-40%	13.2 ± 0.4	0.150 ± 0.003	-0.381 ± 0.005	0.107 ± 0.003	11/21
				40-50%	13.3 ± 0.4	0.147 ± 0.002	-0.376 ± 0.005	0.103 ± 0.003	15/21
				50-60%	12.5 ± 0.3	0.138 ± 0.002	-0.368 ± 0.005	0.100 ± 0.002	28/21
				60-70%	12.3 ± 0.3	0.133 ± 0.002	-0.370 ± 0.005	0.099 ± 0.002	28/19
				70-80%	12.0 ± 0.3	0.128 ± 0.002	-0.365 ± 0.004	0.094 ± 0.002	29/19
Figure 2(b)	π^+	11.5	0-5%	16.1 ± 0.7	0.175 ± 0.003	-0.422 ± 0.005	0.122 ± 0.003	3/21	
			$ y < 0.1$	5-10%	14.5 ± 0.5	0.170 ± 0.003	-0.420 ± 0.005	0.119 ± 0.003	5/21
				10-20%	14.0 ± 0.4	0.166 ± 0.003	-0.417 ± 0.005	0.116 ± 0.003	5/21
				20-30%	12.7 ± 0.3	0.161 ± 0.003	-0.407 ± 0.005	0.115 ± 0.003	4/21
				30-40%	12.2 ± 0.3	0.156 ± 0.003	-0.400 ± 0.005	0.113 ± 0.003	3/21
				40-50%	11.3 ± 0.3	0.149 ± 0.002	-0.391 ± 0.005	0.112 ± 0.003	6/21
				50-60%	11.1 ± 0.3	0.140 ± 0.002	-0.386 ± 0.005	0.108 ± 0.003	10/21
				60-70%	10.8 ± 0.3	0.135 ± 0.002	-0.378 ± 0.005	0.106 ± 0.003	8/19
				70-80%	10.2 ± 0.3	0.129 ± 0.002	-0.374 ± 0.005	0.102 ± 0.003	20/19
Figure 2(c)	K^-	11.5	0-5%	26.9 ± 1.6	0.153 ± 0.003	0.007 ± 0.004	0.114 ± 0.005	1/18	
			$ y < 0.1$	5-10%	24.3 ± 1.4	0.152 ± 0.003	0.011 ± 0.004	0.111 ± 0.005	5/19
				10-20%	22.9 ± 1.2	0.149 ± 0.002	0.012 ± 0.004	0.109 ± 0.005	4/19
				20-30%	21.8 ± 1.1	0.145 ± 0.002	0.015 ± 0.004	0.107 ± 0.005	4/19
				30-40%	20.9 ± 1.0	0.141 ± 0.002	0.022 ± 0.004	0.107 ± 0.005	4/18
				40-50%	17.5 ± 0.7	0.128 ± 0.002	0.032 ± 0.005	0.106 ± 0.005	11/18
				50-60%	15.6 ± 0.6	0.121 ± 0.002	0.051 ± 0.005	0.103 ± 0.005	12/18
				60-70%	15.1 ± 0.6	0.110 ± 0.002	0.064 ± 0.005	0.102 ± 0.005	8/15
				70-80%	15.0 ± 0.5	0.103 ± 0.002	0.076 ± 0.005	0.092 ± 0.004	18/11
Figure 2(d)	K^+	11.5	0-5%	28.3 ± 1.8	0.167 ± 0.003	-0.026 ± 0.004	0.127 ± 0.005	2/20	
			$ y < 0.1$	5-10%	27.4 ± 1.7	0.162 ± 0.003	-0.022 ± 0.004	0.121 ± 0.005	6/21
				10-20%	24.9 ± 1.4	0.158 ± 0.003	-0.009 ± 0.004	0.115 ± 0.005	4/21
				20-30%	23.1 ± 1.3	0.154 ± 0.003	0.003 ± 0.004	0.111 ± 0.005	8/21
				30-40%	18.4 ± 0.8	0.149 ± 0.002	0.014 ± 0.004	0.108 ± 0.005	7/21
				40-50%	17.0 ± 0.7	0.141 ± 0.002	0.019 ± 0.004	0.101 ± 0.005	16/21
				50-60%	14.5 ± 0.5	0.134 ± 0.002	0.022 ± 0.004	0.099 ± 0.004	12/20
				60-70%	13.9 ± 0.4	0.126 ± 0.002	0.032 ± 0.005	0.091 ± 0.004	5/18
				70-80%	13.9 ± 0.4	0.116 ± 0.002	0.041 ± 0.005	0.089 ± 0.004	13/17
Figure 2(e)	\bar{p}	11.5	0-5%	16.1 ± 0.7	0.128 ± 0.002	0.003 ± 0.004	0.346 ± 0.008	19/18	
			$ y < 0.1$	5-10%	15.6 ± 0.6	0.124 ± 0.002	0.006 ± 0.004	0.330 ± 0.008	12/18
				10-20%	15.1 ± 0.6	0.118 ± 0.002	0.010 ± 0.004	0.326 ± 0.008	13/18
				20-30%	14.7 ± 0.5	0.116 ± 0.002	0.012 ± 0.004	0.314 ± 0.008	5/18
				30-40%	14.0 ± 0.4	0.107 ± 0.002	0.015 ± 0.004	0.306 ± 0.008	3/18
				40-50%	13.2 ± 0.4	0.098 ± 0.002	0.017 ± 0.004	0.296 ± 0.007	8/15
				50-60%	12.1 ± 0.3	0.091 ± 0.002	0.020 ± 0.004	0.292 ± 0.007	7/14
				60-70%	11.1 ± 0.3	0.081 ± 0.001	0.021 ± 0.004	0.284 ± 0.007	7/9
				70-80%	10.1 ± 0.3	0.072 ± 0.001	0.022 ± 0.004	0.272 ± 0.007	6/9
Figure 2(f)	p	11.5	0-5%	17.8 ± 0.7	0.129 ± 0.002	0.001 ± 0.004	0.347 ± 0.008	8/23	
			$ y < 0.1$	5-10%	16.2 ± 0.7	0.128 ± 0.002	0.004 ± 0.004	0.333 ± 0.008	2/24
				10-20%	14.9 ± 0.5	0.122 ± 0.002	0.011 ± 0.004	0.327 ± 0.008	5/24
				20-30%	13.8 ± 0.4	0.119 ± 0.002	0.013 ± 0.004	0.314 ± 0.008	7/24
				30-40%	13.1 ± 0.4	0.115 ± 0.002	0.015 ± 0.004	0.302 ± 0.008	12/24
				40-50%	12.4 ± 0.3	0.108 ± 0.002	0.017 ± 0.004	0.290 ± 0.007	11/23
				50-60%	11.7 ± 0.3	0.104 ± 0.002	0.018 ± 0.004	0.274 ± 0.007	14/23
				60-70%	11.1 ± 0.3	0.094 ± 0.002	0.021 ± 0.004	0.260 ± 0.007	18/23
				70-80%	10.1 ± 0.3	0.072 ± 0.001	0.022 ± 0.004	0.250 ± 0.007	18/23

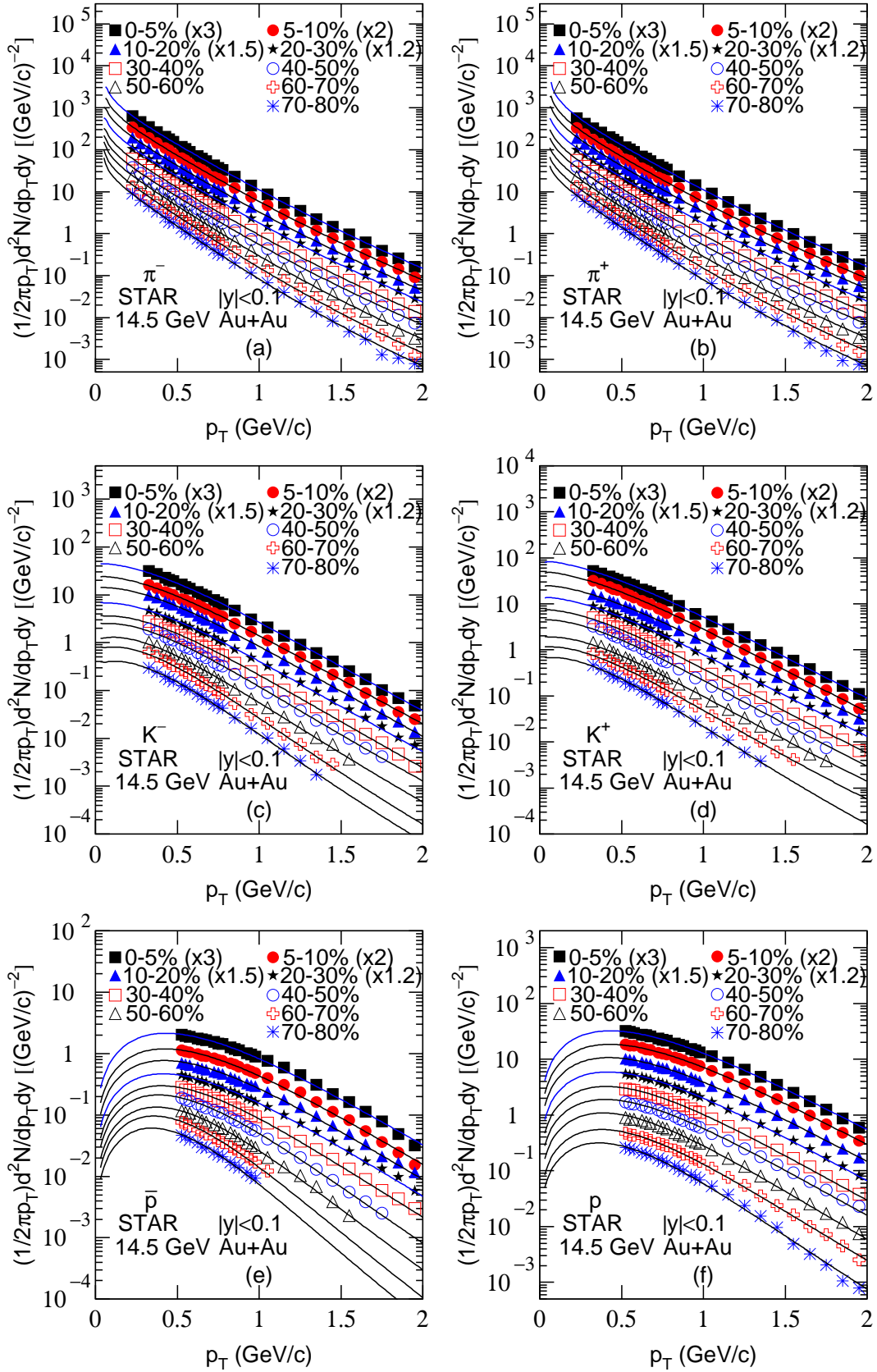


Figure 3. Same as Figure 1, but showing the results for 14.5 GeV Au-Au collisions. The symbols represent the STAR data [34].

Table 3. Values of n , T_0 , a_0 , $\langle\beta_t\rangle$, χ^2 , and ndof corresponding to the curves in Figure 3.

Figure	Particle	$\sqrt{s_{NN}}$ (GeV)	Selection	n	T_0 (GeV)	a_0	$\langle\beta_t\rangle$ (c)	χ^2/ndof	
Figure 3(a)	π^-	14.5	0-5%	14.3 ± 0.5	0.171 ± 0.003	-0.407 ± 0.005	0.117 ± 0.003	1/23	
			$ y < 0.1$	5-10%	12.6 ± 0.3	0.165 ± 0.003	-0.405 ± 0.005	0.114 ± 0.003	2/23
			10-20%	11.9 ± 0.3	0.161 ± 0.003	-0.396 ± 0.005	0.112 ± 0.003	3/23	
			20-30%	11.5 ± 0.3	0.158 ± 0.003	-0.392 ± 0.005	0.110 ± 0.003	4/23	
			30-40%	11.0 ± 0.3	0.153 ± 0.003	-0.385 ± 0.005	0.108 ± 0.003	4/23	
			40-50%	10.8 ± 0.3	0.150 ± 0.003	-0.378 ± 0.005	0.104 ± 0.003	3/23	
			50-60%	10.7 ± 0.3	0.141 ± 0.002	-0.377 ± 0.005	0.102 ± 0.003	13/23	
			60-70%	10.4 ± 0.3	0.133 ± 0.002	-0.370 ± 0.005	0.101 ± 0.003	25/23	
			70-80%	10.3 ± 0.3	0.128 ± 0.002	-0.368 ± 0.004	0.098 ± 0.002	25/23	
Figure 3(b)	π^+	14.5	0-5%	14.6 ± 0.5	0.179 ± 0.003	-0.424 ± 0.005	0.124 ± 0.003	5/23	
			$ y < 0.1$	5-10%	12.7 ± 0.3	0.172 ± 0.003	-0.421 ± 0.005	0.122 ± 0.003	2/23
			10-20%	11.9 ± 0.3	0.167 ± 0.003	-0.419 ± 0.005	0.120 ± 0.003	4/23	
			20-30%	11.4 ± 0.3	0.163 ± 0.003	-0.416 ± 0.005	0.116 ± 0.003	4/23	
			30-40%	10.9 ± 0.3	0.159 ± 0.003	-0.411 ± 0.005	0.114 ± 0.003	3/23	
			40-50%	10.4 ± 0.3	0.151 ± 0.003	-0.404 ± 0.005	0.112 ± 0.003	1/23	
			50-60%	10.2 ± 0.3	0.143 ± 0.002	-0.396 ± 0.005	0.110 ± 0.003	7/23	
			60-70%	10.0 ± 0.3	0.137 ± 0.002	-0.394 ± 0.005	0.108 ± 0.003	14/23	
			70-80%	9.9 ± 0.2	0.129 ± 0.002	-0.384 ± 0.005	0.105 ± 0.003	26/23	
Figure 3(c)	K^-	14.5	0-5%	23.3 ± 1.3	0.159 ± 0.003	-0.015 ± 0.004	0.116 ± 0.005	2/21	
			$ y < 0.1$	5-10%	20.8 ± 1.0	0.157 ± 0.003	-0.013 ± 0.004	0.113 ± 0.005	2/21
			10-20%	20.3 ± 1.0	0.152 ± 0.003	0.002 ± 0.004	0.112 ± 0.005	2/21	
			20-30%	18.9 ± 0.8	0.148 ± 0.002	0.014 ± 0.004	0.113 ± 0.005	7/21	
			30-40%	18.4 ± 0.8	0.143 ± 0.002	0.026 ± 0.004	0.107 ± 0.005	6/21	
			40-50%	13.7 ± 0.4	0.130 ± 0.002	0.029 ± 0.004	0.105 ± 0.005	5/19	
			50-60%	14.0 ± 0.4	0.122 ± 0.002	0.044 ± 0.005	0.102 ± 0.005	6/17	
			60-70%	13.2 ± 0.3	0.109 ± 0.002	0.053 ± 0.005	0.101 ± 0.005	6/16	
			70-80%	12.1 ± 0.3	0.104 ± 0.002	0.062 ± 0.005	0.098 ± 0.004	3/15	
Figure 3(d)	K^+	14.5	0-5%	26.6 ± 1.6	0.170 ± 0.003	-0.037 ± 0.005	0.129 ± 0.005	0.9/21	
			$ y < 0.1$	5-10%	22.1 ± 1.2	0.163 ± 0.003	-0.034 ± 0.005	0.125 ± 0.005	3/21
			10-20%	17.8 ± 0.7	0.162 ± 0.003	-0.024 ± 0.004	0.123 ± 0.005	1/21	
			20-30%	16.7 ± 0.7	0.158 ± 0.003	-0.020 ± 0.004	0.112 ± 0.005	2/21	
			30-40%	15.9 ± 0.6	0.151 ± 0.003	-0.017 ± 0.004	0.108 ± 0.005	5/21	
			40-50%	13.6 ± 0.4	0.142 ± 0.002	-0.008 ± 0.004	0.105 ± 0.005	10/19	
			50-60%	11.8 ± 0.3	0.137 ± 0.002	0.012 ± 0.004	0.101 ± 0.005	6/19	
			60-70%	11.3 ± 0.3	0.127 ± 0.002	0.015 ± 0.004	0.095 ± 0.004	4/17	
			70-80%	12.3 ± 0.3	0.115 ± 0.002	0.025 ± 0.004	0.091 ± 0.004	2/15	
Figure 3(e)	\bar{p}	14.5	0-5%	15.9 ± 0.6	0.127 ± 0.002	0.001 ± 0.004	0.358 ± 0.008	8/20	
			$ y < 0.1$	5-10%	14.6 ± 0.5	0.124 ± 0.002	0.004 ± 0.004	0.344 ± 0.008	9/20
			10-20%	13.7 ± 0.4	0.120 ± 0.002	0.008 ± 0.004	0.339 ± 0.008	7/20	
			20-30%	13.3 ± 0.4	0.117 ± 0.002	0.011 ± 0.004	0.333 ± 0.008	5/20	
			30-40%	11.5 ± 0.3	0.108 ± 0.002	0.014 ± 0.004	0.324 ± 0.008	5/20	
			40-50%	11.7 ± 0.3	0.097 ± 0.002	0.016 ± 0.004	0.318 ± 0.008	2/18	
			50-60%	11.7 ± 0.3	0.089 ± 0.001	0.018 ± 0.004	0.312 ± 0.008	4/16	
			60-70%	10.5 ± 0.3	0.078 ± 0.001	0.020 ± 0.004	0.306 ± 0.008	3/11	
			70-80%	9.9 ± 0.2	0.073 ± 0.001	0.021 ± 0.004	0.298 ± 0.007	3/10	
Figure 3(f)	p	14.5	0-5%	17.0 ± 0.7	0.133 ± 0.002	-0.001 ± 0.004	0.350 ± 0.008	1/20	
			$ y < 0.1$	5-10%	15.4 ± 0.6	0.131 ± 0.002	0.001 ± 0.004	0.343 ± 0.008	0.9/20
			10-20%	13.8 ± 0.4	0.126 ± 0.002	0.008 ± 0.004	0.331 ± 0.008	0.9/20	
			20-30%	13.1 ± 0.4	0.122 ± 0.002	0.011 ± 0.004	0.318 ± 0.008	2/20	
			30-40%	12.6 ± 0.3	0.118 ± 0.002	0.014 ± 0.004	0.304 ± 0.008	3/20	
			40-50%	12.1 ± 0.3	0.116 ± 0.002	0.016 ± 0.004	0.298 ± 0.007	7/20	
			50-60%	11.5 ± 0.3	0.107 ± 0.002	0.017 ± 0.004	0.290 ± 0.007	7/20	
			60-70%	10.9 ± 0.3	0.103 ± 0.002	0.020 ± 0.004	0.283 ± 0.007	4/20	
			70-80%	10.3 ± 0.3	0.099 ± 0.002	0.023 ± 0.004	0.278 ± 0.007	4/20	

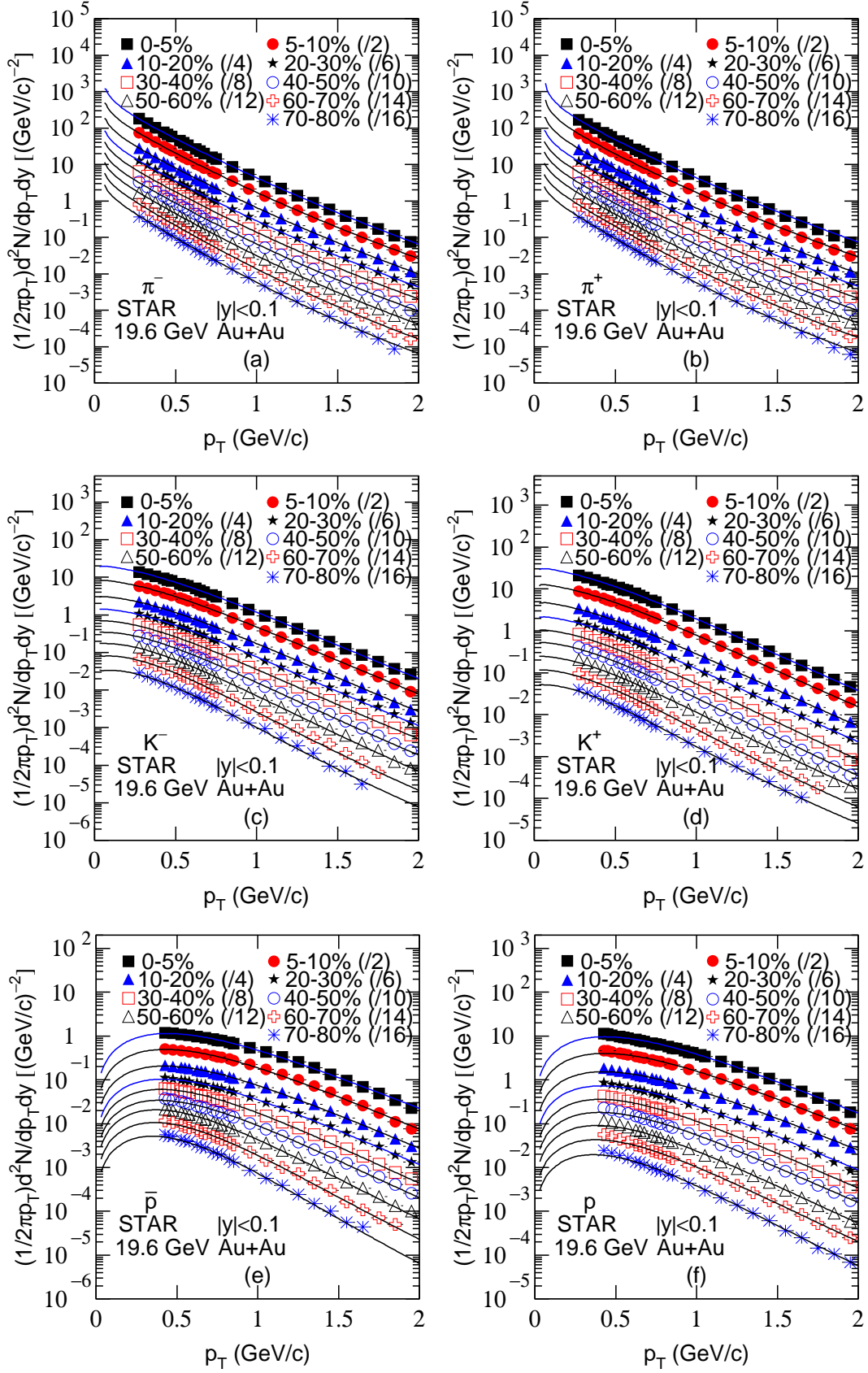


Figure 4. Same as Figure 1, but showing the results for 19.6 GeV Au-Au collisions. The symbols represent the STAR data [33].

Table 4. Values of n , T_0 , a_0 , $\langle\beta_t\rangle$, χ^2 , and ndof corresponding to the curves in Figure 4.

Figure	Particle	$\sqrt{s_{NN}}$ (GeV)	Selection	n	T_0 (GeV)	a_0	$\langle\beta_t\rangle$ (c)	χ^2/ndof	
Figure 4(a)	π^-	19.6	0-5%	12.9 ± 0.3	0.173 ± 0.003	-0.410 ± 0.005	0.119 ± 0.003	1/21	
			$ y < 0.1$	5-10%	11.5 ± 0.3	0.168 ± 0.003	-0.409 ± 0.005	0.117 ± 0.003	2/21
			10-20%	10.9 ± 0.3	0.164 ± 0.003	-0.402 ± 0.005	0.115 ± 0.003	2/21	
			20-30%	10.3 ± 0.3	0.161 ± 0.003	-0.404 ± 0.005	0.112 ± 0.003	2/21	
			30-40%	10.0 ± 0.3	0.157 ± 0.003	-0.395 ± 0.005	0.109 ± 0.003	3/21	
			40-50%	9.8 ± 0.2	0.153 ± 0.003	-0.390 ± 0.005	0.107 ± 0.003	3/21	
			50-60%	9.4 ± 0.2	0.145 ± 0.002	-0.383 ± 0.005	0.104 ± 0.003	4/21	
			60-70%	9.0 ± 0.2	0.136 ± 0.002	-0.377 ± 0.005	0.103 ± 0.003	13/21	
			70-80%	8.9 ± 0.2	0.131 ± 0.002	-0.372 ± 0.005	0.102 ± 0.003	13/20	
Figure 4(b)	π^+	19.6	0-5%	12.9 ± 0.3	0.183 ± 0.003	-0.424 ± 0.005	0.125 ± 0.003	14/21	
			$ y < 0.1$	5-10%	11.9 ± 0.3	0.177 ± 0.003	-0.420 ± 0.005	0.124 ± 0.003	6/21
			10-20%	11.4 ± 0.3	0.170 ± 0.003	-0.417 ± 0.005	0.121 ± 0.003	1/21	
			20-30%	10.6 ± 0.3	0.166 ± 0.003	-0.415 ± 0.005	0.119 ± 0.003	1/21	
			30-40%	10.3 ± 0.3	0.162 ± 0.003	-0.414 ± 0.005	0.115 ± 0.003	2/21	
			40-50%	9.3 ± 0.2	0.153 ± 0.003	-0.409 ± 0.005	0.114 ± 0.003	3/21	
			50-60%	8.8 ± 0.2	0.146 ± 0.002	-0.401 ± 0.005	0.113 ± 0.003	5/21	
			60-70%	8.7 ± 0.2	0.139 ± 0.002	-0.395 ± 0.005	0.111 ± 0.003	4/21	
			70-80%	8.6 ± 0.2	0.132 ± 0.002	-0.387 ± 0.005	0.109 ± 0.003	18/21	
Figure 4(c)	K^-	19.6	0-5%	21.1 ± 1.1	0.165 ± 0.003	-0.034 ± 0.005	0.124 ± 0.005	2/21	
			$ y < 0.1$	5-10%	19.3 ± 0.9	0.161 ± 0.003	-0.030 ± 0.005	0.121 ± 0.005	2/21
			10-20%	17.9 ± 0.8	0.155 ± 0.003	-0.018 ± 0.004	0.119 ± 0.005	3/21	
			20-30%	16.5 ± 0.7	0.151 ± 0.003	-0.016 ± 0.004	0.115 ± 0.005	7/21	
			30-40%	14.4 ± 0.5	0.144 ± 0.002	-0.009 ± 0.004	0.114 ± 0.005	12/21	
			40-50%	13.3 ± 0.4	0.133 ± 0.002	0.012 ± 0.004	0.106 ± 0.005	12/20	
			50-60%	13.1 ± 0.4	0.126 ± 0.002	0.016 ± 0.004	0.103 ± 0.005	18/20	
			60-70%	11.0 ± 0.3	0.111 ± 0.002	0.032 ± 0.005	0.102 ± 0.005	30/18	
			70-80%	10.3 ± 0.3	0.105 ± 0.002	0.044 ± 0.005	0.102 ± 0.005	25/16	
Figure 4(d)	K^+	19.6	0-5%	22.7 ± 1.2	0.172 ± 0.003	-0.045 ± 0.005	0.132 ± 0.005	1/21	
			$ y < 0.1$	5-10%	19.2 ± 0.9	0.168 ± 0.003	-0.034 ± 0.005	0.128 ± 0.005	3/21
			10-20%	17.2 ± 0.7	0.164 ± 0.003	-0.030 ± 0.005	0.119 ± 0.005	3/21	
			20-30%	15.6 ± 0.6	0.159 ± 0.003	-0.026 ± 0.004	0.115 ± 0.005	5/21	
			30-40%	15.1 ± 0.6	0.151 ± 0.003	-0.020 ± 0.004	0.109 ± 0.005	15/21	
			40-50%	14.4 ± 0.5	0.145 ± 0.002	-0.017 ± 0.004	0.105 ± 0.005	14/20	
			50-60%	12.5 ± 0.3	0.141 ± 0.002	-0.011 ± 0.004	0.102 ± 0.005	23/20	
			60-70%	9.9 ± 0.2	0.127 ± 0.002	-0.006 ± 0.004	0.099 ± 0.004	15/18	
			70-80%	7.9 ± 0.2	0.115 ± 0.002	0.007 ± 0.004	0.093 ± 0.004	10/17	
Figure 4(e)	\bar{p}	19.6	0-5%	15.3 ± 0.6	0.132 ± 0.002	0.001 ± 0.004	0.367 ± 0.008	5/17	
			$ y < 0.1$	5-10%	14.3 ± 0.5	0.126 ± 0.002	0.003 ± 0.004	0.353 ± 0.008	9/17
			10-20%	13.2 ± 0.4	0.123 ± 0.002	0.006 ± 0.004	0.341 ± 0.008	5/19	
			20-30%	12.8 ± 0.3	0.120 ± 0.002	0.009 ± 0.004	0.328 ± 0.008	3/19	
			30-40%	12.4 ± 0.3	0.111 ± 0.002	0.013 ± 0.004	0.315 ± 0.008	5/20	
			40-50%	11.0 ± 0.3	0.106 ± 0.002	0.014 ± 0.004	0.305 ± 0.008	7/20	
			50-60%	10.2 ± 0.3	0.094 ± 0.001	0.015 ± 0.004	0.299 ± 0.008	11/20	
			60-70%	9.7 ± 0.2	0.086 ± 0.001	0.017 ± 0.004	0.301 ± 0.008	9/18	
			70-80%	9.5 ± 0.2	0.080 ± 0.001	0.019 ± 0.004	0.284 ± 0.007	11/17	
Figure 4(f)	p	19.6	0-5%	15.9 ± 0.6	0.133 ± 0.002	-0.002 ± 0.004	0.355 ± 0.008	7/24	
			$ y < 0.1$	5-10%	14.4 ± 0.5	0.132 ± 0.002	0.001 ± 0.004	0.345 ± 0.008	6/20
			10-20%	13.3 ± 0.4	0.129 ± 0.002	0.005 ± 0.004	0.339 ± 0.008	5/18	
			20-30%	12.7 ± 0.3	0.122 ± 0.002	0.007 ± 0.004	0.328 ± 0.008	9/18	
			30-40%	12.3 ± 0.3	0.117 ± 0.002	0.010 ± 0.004	0.316 ± 0.008	8/18	
			40-50%	11.9 ± 0.3	0.116 ± 0.002	0.013 ± 0.004	0.305 ± 0.008	12/18	
			50-60%	11.3 ± 0.3	0.109 ± 0.002	0.015 ± 0.004	0.286 ± 0.007	15/18	
			60-70%	10.6 ± 0.3	0.104 ± 0.002	0.017 ± 0.004	0.280 ± 0.007	16/18	
			70-80%	10.3 ± 0.3	0.104 ± 0.002	0.017 ± 0.004	0.280 ± 0.007	16/18	

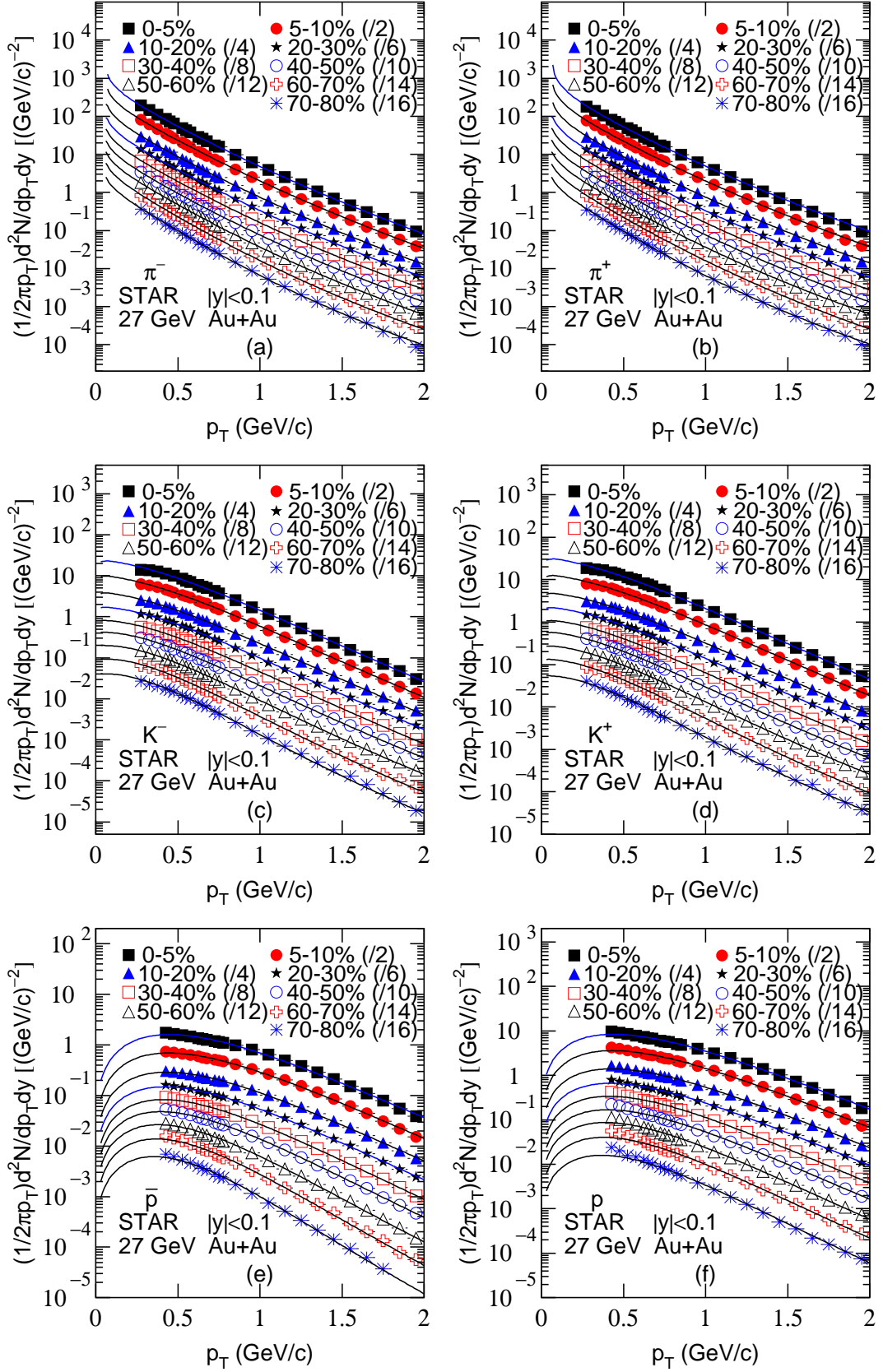


Figure 5. Same as Figure 1, but showing the results for 27 GeV Au-Au collisions. The symbols represent the STAR data [33].

Table 5. Values of n , T_0 , a_0 , $\langle\beta_t\rangle$, χ^2 , and ndof corresponding to the curves in Figure 5.

Figure	Particle	$\sqrt{s_{NN}}$ (GeV)	Selection	n	T_0 (GeV)	a_0	$\langle\beta_t\rangle$ (c)	χ^2/ndof	
Figure 5(a)	π^-	27	0-5%	11.8 ± 0.3	0.175 ± 0.003	-0.410 ± 0.005	0.121 ± 0.003	4/21	
			$ y < 0.1$	5-10%	10.8 ± 0.3	0.170 ± 0.003	-0.409 ± 0.005	0.119 ± 0.003	1/21
				10-20%	10.1 ± 0.3	0.167 ± 0.003	-0.407 ± 0.005	0.118 ± 0.003	2/21
				20-30%	9.5 ± 0.2	0.164 ± 0.003	-0.405 ± 0.005	0.116 ± 0.003	1/21
				30-40%	8.9 ± 0.2	0.160 ± 0.003	-0.403 ± 0.005	0.112 ± 0.003	1/21
				40-50%	8.4 ± 0.2	0.155 ± 0.003	-0.398 ± 0.005	0.109 ± 0.003	3/21
				50-60%	8.1 ± 0.2	0.148 ± 0.002	-0.388 ± 0.005	0.107 ± 0.003	2/21
				60-70%	7.7 ± 0.2	0.139 ± 0.002	-0.385 ± 0.005	0.106 ± 0.003	4/21
				70-80%	7.6 ± 0.2	0.133 ± 0.002	-0.373 ± 0.005	0.105 ± 0.003	13/21
Figure 5(b)	π^+	27	0-5%	11.7 ± 0.3	0.186 ± 0.003	-0.425 ± 0.005	0.126 ± 0.003	14/21	
			$ y < 0.1$	5-10%	11.2 ± 0.3	0.180 ± 0.003	-0.424 ± 0.005	0.124 ± 0.003	6/21
				10-20%	9.9 ± 0.2	0.172 ± 0.003	-0.421 ± 0.005	0.122 ± 0.003	3/21
				20-30%	9.8 ± 0.2	0.168 ± 0.003	-0.416 ± 0.005	0.120 ± 0.003	1/21
				30-40%	9.6 ± 0.2	0.164 ± 0.003	-0.415 ± 0.005	0.118 ± 0.003	1/21
				40-50%	8.6 ± 0.2	0.156 ± 0.003	-0.409 ± 0.005	0.115 ± 0.003	1/21
				50-60%	7.9 ± 0.2	0.149 ± 0.002	-0.402 ± 0.005	0.116 ± 0.003	4/21
				60-70%	7.8 ± 0.2	0.142 ± 0.002	-0.396 ± 0.005	0.113 ± 0.003	4/21
				70-80%	7.3 ± 0.2	0.135 ± 0.002	-0.395 ± 0.005	0.112 ± 0.003	9/21
Figure 5(c)	K^-	27	0-5%	21.0 ± 1.0	0.166 ± 0.003	-0.038 ± 0.005	0.136 ± 0.005	12/20	
			$ y < 0.1$	5-10%	18.5 ± 0.8	0.164 ± 0.003	-0.036 ± 0.005	0.129 ± 0.005	4/21
				10-20%	15.6 ± 0.6	0.158 ± 0.003	-0.028 ± 0.004	0.128 ± 0.005	4/21
				20-30%	13.7 ± 0.4	0.152 ± 0.003	-0.019 ± 0.004	0.126 ± 0.005	5/21
				30-40%	12.6 ± 0.3	0.148 ± 0.002	-0.010 ± 0.004	0.116 ± 0.005	5/21
				40-50%	10.2 ± 0.3	0.137 ± 0.002	-0.002 ± 0.004	0.111 ± 0.005	6/21
				50-60%	9.4 ± 0.2	0.128 ± 0.002	0.009 ± 0.005	0.110 ± 0.005	6/21
				60-70%	8.9 ± 0.2	0.120 ± 0.002	0.014 ± 0.004	0.105 ± 0.005	10/21
				70-80%	8.6 ± 0.2	0.111 ± 0.002	0.018 ± 0.004	0.105 ± 0.005	22/21
Figure 5(d)	K^+	27	0-5%	21.9 ± 1.1	0.175 ± 0.003	-0.050 ± 0.005	0.144 ± 0.005	12/21	
			$ y < 0.1$	5-10%	19.2 ± 0.9	0.171 ± 0.003	-0.035 ± 0.005	0.137 ± 0.005	7/21
				10-20%	17.2 ± 0.7	0.167 ± 0.003	-0.029 ± 0.004	0.133 ± 0.005	7/21
				20-30%	13.4 ± 0.4	0.162 ± 0.003	-0.026 ± 0.004	0.126 ± 0.005	3/21
				30-40%	11.0 ± 0.3	0.152 ± 0.003	-0.022 ± 0.004	0.123 ± 0.005	3/21
				40-50%	9.5 ± 0.2	0.143 ± 0.002	-0.019 ± 0.004	0.115 ± 0.005	4/21
				50-60%	9.1 ± 0.2	0.138 ± 0.002	-0.015 ± 0.004	0.109 ± 0.005	5/21
				60-70%	8.6 ± 0.2	0.129 ± 0.002	-0.012 ± 0.004	0.102 ± 0.005	6/21
				70-80%	7.5 ± 0.2	0.119 ± 0.002	-0.004 ± 0.004	0.096 ± 0.004	13/21
Figure 5(e)	\bar{p}	27	0-5%	14.6 ± 0.5	0.134 ± 0.002	-0.001 ± 0.004	0.379 ± 0.008	5/17	
			$ y < 0.1$	5-10%	14.0 ± 0.4	0.130 ± 0.002	0.003 ± 0.004	0.375 ± 0.008	4/17
				10-20%	12.4 ± 0.3	0.127 ± 0.002	0.005 ± 0.004	0.356 ± 0.008	3/17
				20-30%	11.3 ± 0.3	0.124 ± 0.002	0.008 ± 0.004	0.330 ± 0.008	2/17
				30-40%	10.7 ± 0.3	0.115 ± 0.002	0.011 ± 0.004	0.328 ± 0.008	3/17
				40-50%	9.8 ± 0.2	0.110 ± 0.002	0.015 ± 0.004	0.304 ± 0.008	3/17
				50-60%	9.2 ± 0.2	0.097 ± 0.002	0.016 ± 0.004	0.307 ± 0.008	7/17
				60-70%	8.9 ± 0.2	0.090 ± 0.002	0.018 ± 0.004	0.300 ± 0.007	10/17
				70-80%	8.8 ± 0.2	0.084 ± 0.001	0.019 ± 0.004	0.285 ± 0.007	10/15
Figure 5(f)	p	27	0-5%	14.7 ± 0.5	0.136 ± 0.002	-0.005 ± 0.004	0.359 ± 0.008	6/18	
			$ y < 0.1$	5-10%	13.7 ± 0.4	0.133 ± 0.002	-0.003 ± 0.004	0.349 ± 0.008	6/18
				10-20%	13.1 ± 0.4	0.130 ± 0.002	0.004 ± 0.004	0.339 ± 0.008	5/18
				20-30%	11.6 ± 0.3	0.124 ± 0.002	0.005 ± 0.004	0.333 ± 0.008	6/18
				30-40%	12.0 ± 0.3	0.119 ± 0.002	0.007 ± 0.004	0.328 ± 0.008	8/18
				40-50%	12.1 ± 0.3	0.118 ± 0.002	0.011 ± 0.004	0.311 ± 0.008	13/18
				50-60%	10.7 ± 0.3	0.109 ± 0.002	0.013 ± 0.004	0.298 ± 0.007	15/18
				60-70%	10.0 ± 0.3	0.105 ± 0.002	0.016 ± 0.004	0.283 ± 0.007	20/18
				70-80%	9.9 ± 0.3	0.105 ± 0.002	0.016 ± 0.004	0.283 ± 0.007	20/18

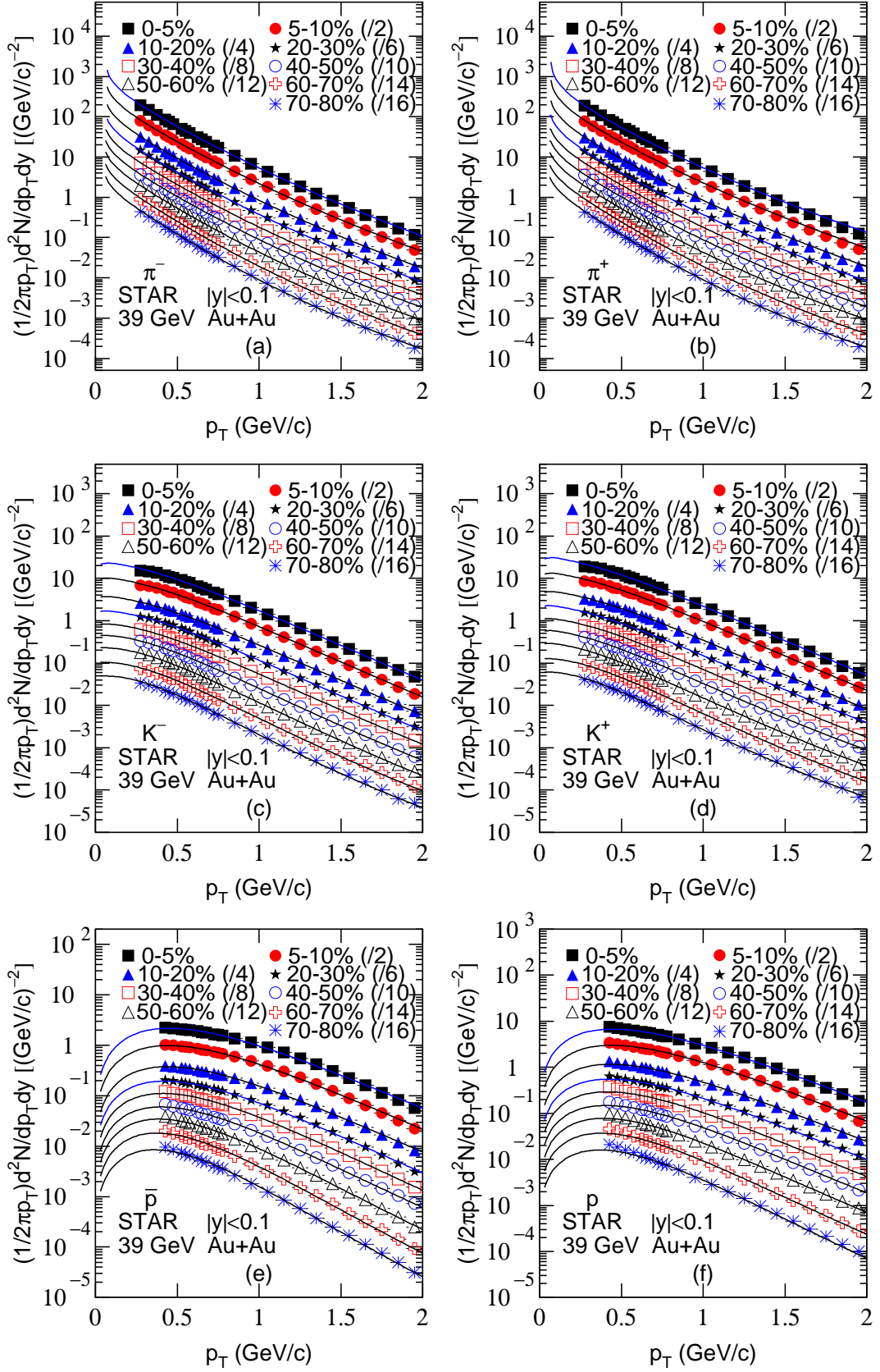


Figure 6. Same as Figure 1, but showing the results for 39 GeV Au-Au collisions. The symbols represent the STAR data [33].

Table 6. Values of n , T_0 , a_0 , $\langle\beta_t\rangle$, χ^2 , and ndof corresponding to the curves in Figure 6.

Figure	Particle	$\sqrt{s_{NN}}$ (GeV)	Selection	n	T_0 (GeV)	a_0	$\langle\beta_t\rangle$ (c)	χ^2/ndof	
Figure 6(a)	π^-	39	0-5%	10.1 ± 0.3	0.179 ± 0.003	-0.418 ± 0.005	0.122 ± 0.003	2/21	
			$ y < 0.1$	5-10%	9.2 ± 0.2	0.173 ± 0.003	-0.414 ± 0.005	0.120 ± 0.003	2/21
				10-20%	8.8 ± 0.2	0.170 ± 0.003	-0.412 ± 0.005	0.118 ± 0.003	1/21
				20-30%	8.3 ± 0.2	0.167 ± 0.003	-0.411 ± 0.005	0.115 ± 0.003	1/21
				30-40%	7.9 ± 0.2	0.162 ± 0.003	-0.403 ± 0.005	0.113 ± 0.003	1/21
				40-50%	7.6 ± 0.2	0.158 ± 0.003	-0.399 ± 0.005	0.107 ± 0.003	1/21
				50-60%	7.1 ± 0.2	0.150 ± 0.003	-0.394 ± 0.005	0.106 ± 0.003	1/21
				60-70%	6.7 ± 0.1	0.142 ± 0.002	-0.391 ± 0.005	0.105 ± 0.003	3/21
				70-80%	6.5 ± 0.1	0.136 ± 0.002	-0.384 ± 0.005	0.104 ± 0.003	6/21
Figure 6(b)	π^+	39	0-5%	9.2 ± 0.2	0.190 ± 0.003	-0.428 ± 0.005	0.126 ± 0.003	28/21	
			$ y < 0.1$	5-10%	8.8 ± 0.2	0.183 ± 0.003	-0.426 ± 0.005	0.125 ± 0.003	19/21
				10-20%	8.4 ± 0.2	0.175 ± 0.003	-0.422 ± 0.005	0.123 ± 0.003	5/21
				20-30%	8.1 ± 0.2	0.170 ± 0.003	-0.418 ± 0.005	0.122 ± 0.003	2/21
				30-40%	7.9 ± 0.2	0.166 ± 0.003	-0.417 ± 0.005	0.119 ± 0.003	1/21
				40-50%	7.3 ± 0.2	0.158 ± 0.003	-0.411 ± 0.005	0.118 ± 0.003	2/21
				50-60%	6.9 ± 0.1	0.151 ± 0.003	-0.406 ± 0.005	0.114 ± 0.003	1/21
				60-70%	6.5 ± 0.1	0.144 ± 0.002	-0.403 ± 0.005	0.112 ± 0.003	3/21
				70-80%	6.1 ± 0.1	0.137 ± 0.002	-0.399 ± 0.005	0.111 ± 0.003	5/21
Figure 6(c)	K^-	39	0-5%	19.8 ± 0.9	0.171 ± 0.003	-0.039 ± 0.005	0.164 ± 0.005	6/21	
			$ y < 0.1$	5-10%	17.8 ± 0.7	0.167 ± 0.003	-0.033 ± 0.005	0.152 ± 0.005	5/21
				10-20%	15.6 ± 0.6	0.165 ± 0.003	-0.024 ± 0.004	0.142 ± 0.005	3/21
				20-30%	14.4 ± 0.5	0.161 ± 0.003	-0.019 ± 0.004	0.137 ± 0.005	5/21
				30-40%	11.4 ± 0.3	0.152 ± 0.003	-0.009 ± 0.004	0.133 ± 0.005	5/21
				40-50%	9.7 ± 0.2	0.139 ± 0.002	-0.005 ± 0.004	0.130 ± 0.005	7/21
				50-60%	9.0 ± 0.2	0.132 ± 0.002	-0.002 ± 0.004	0.126 ± 0.005	9/21
				60-70%	7.8 ± 0.2	0.124 ± 0.002	0.008 ± 0.004	0.123 ± 0.005	11/21
				70-80%	7.0 ± 0.1	0.115 ± 0.002	0.016 ± 0.004	0.113 ± 0.005	15/21
Figure 6(d)	K^+	39	0-5%	20.6 ± 1.0	0.177 ± 0.003	-0.051 ± 0.005	0.150 ± 0.005	8/21	
			$ y < 0.1$	5-10%	18.7 ± 0.8	0.175 ± 0.003	-0.042 ± 0.005	0.145 ± 0.005	4/21
				10-20%	15.3 ± 0.6	0.169 ± 0.003	-0.030 ± 0.005	0.138 ± 0.005	3/21
				20-30%	11.4 ± 0.3	0.164 ± 0.003	-0.029 ± 0.004	0.128 ± 0.005	3/21
				30-40%	10.3 ± 0.3	0.157 ± 0.003	-0.024 ± 0.004	0.122 ± 0.005	3/21
				40-50%	7.9 ± 0.2	0.145 ± 0.002	-0.021 ± 0.004	0.119 ± 0.005	3/21
				50-60%	7.6 ± 0.2	0.138 ± 0.002	-0.019 ± 0.004	0.117 ± 0.005	7/21
				60-70%	7.1 ± 0.2	0.132 ± 0.002	-0.008 ± 0.004	0.115 ± 0.005	5/21
				70-80%	6.1 ± 0.1	0.121 ± 0.002	-0.003 ± 0.004	0.106 ± 0.005	9/21
Figure 6(e)	\bar{p}	39	0-5%	13.1 ± 0.4	0.135 ± 0.002	-0.002 ± 0.004	0.387 ± 0.008	7/18	
			$ y < 0.1$	5-10%	12.7 ± 0.3	0.130 ± 0.002	0.003 ± 0.004	0.378 ± 0.008	5/18
				10-20%	11.9 ± 0.3	0.128 ± 0.002	0.004 ± 0.004	0.370 ± 0.008	4/18
				20-30%	11.3 ± 0.3	0.124 ± 0.002	0.005 ± 0.004	0.340 ± 0.008	5/18
				30-40%	10.5 ± 0.3	0.117 ± 0.002	0.007 ± 0.004	0.334 ± 0.008	3/18
				40-50%	9.0 ± 0.2	0.111 ± 0.002	0.008 ± 0.004	0.322 ± 0.008	3/18
				50-60%	8.7 ± 0.2	0.101 ± 0.002	0.010 ± 0.004	0.316 ± 0.008	5/18
				60-70%	8.1 ± 0.2	0.091 ± 0.002	0.012 ± 0.004	0.314 ± 0.008	7/18
				70-80%	8.0 ± 0.2	0.088 ± 0.001	0.015 ± 0.004	0.290 ± 0.007	7/18
Figure 6(f)	p	39	0-5%	13.9 ± 0.4	0.139 ± 0.002	-0.007 ± 0.004	0.376 ± 0.008	3/17	
			$ y < 0.1$	5-10%	13.1 ± 0.4	0.135 ± 0.002	-0.004 ± 0.004	0.365 ± 0.008	5/17
				10-20%	11.8 ± 0.3	0.133 ± 0.002	0.001 ± 0.004	0.350 ± 0.008	3/17
				20-30%	10.3 ± 0.3	0.127 ± 0.002	0.003 ± 0.004	0.341 ± 0.008	4/17
				30-40%	9.9 ± 0.2	0.121 ± 0.002	0.005 ± 0.004	0.332 ± 0.008	8/17
				40-50%	9.5 ± 0.2	0.120 ± 0.002	0.007 ± 0.004	0.310 ± 0.008	6/17
				50-60%	8.9 ± 0.2	0.111 ± 0.002	0.009 ± 0.004	0.303 ± 0.008	8/17
				60-70%	8.5 ± 0.2	0.104 ± 0.002	0.011 ± 0.004	0.288 ± 0.007	9/17
				70-80%	8.0 ± 0.2	0.098 ± 0.002	0.013 ± 0.004	0.280 ± 0.007	9/17

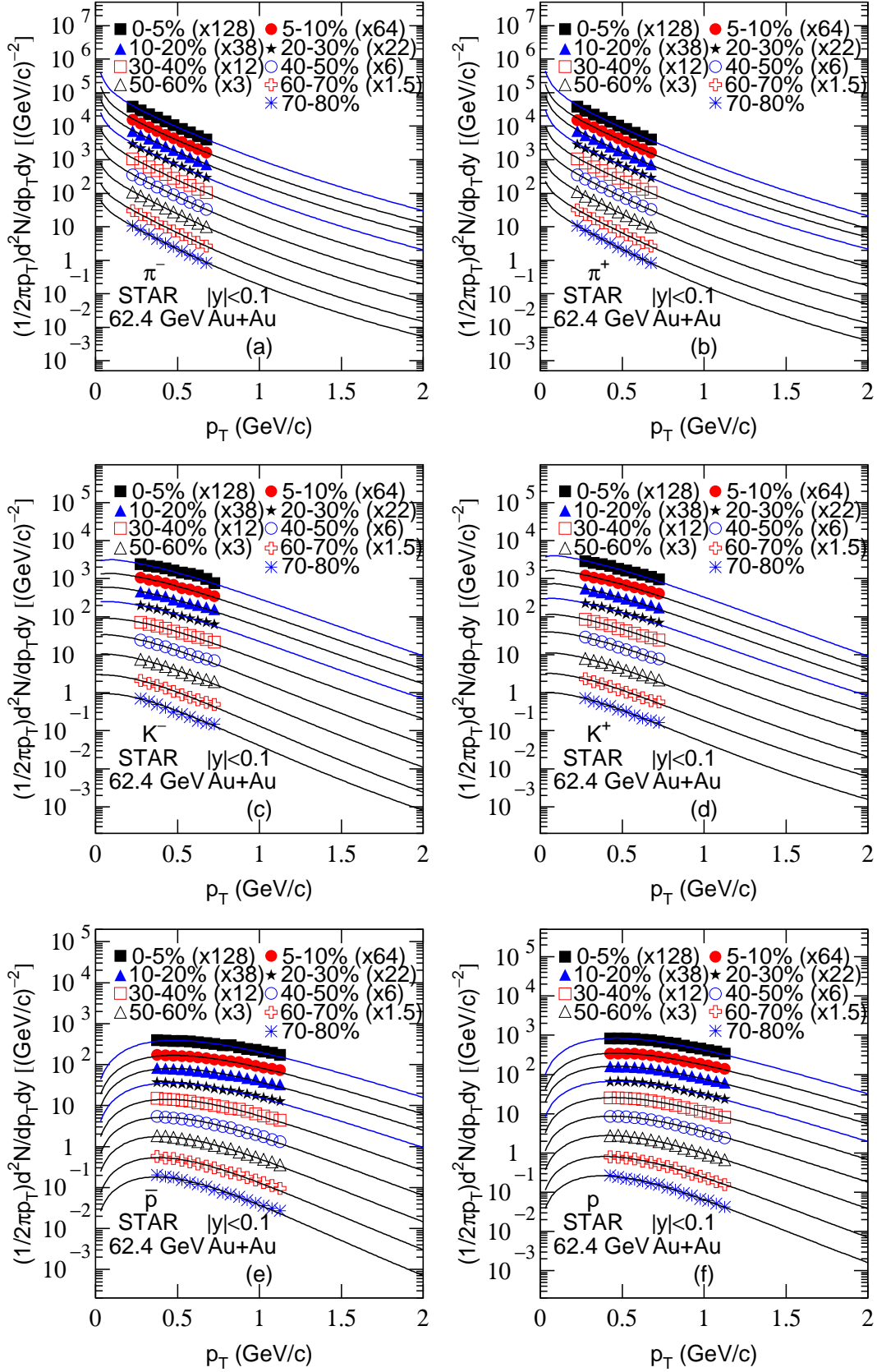


Figure 7. Same as Figure 1, but showing the results for 62.4 GeV Au-Au collisions. The symbols represent the STAR data [35].

Table 7. Values of n , T_0 , a_0 , $\langle \beta_t \rangle$, χ^2 , and ndof corresponding to the curves in Figure 7.

Figure	Particle	$\sqrt{s_{NN}}$ (GeV)	Selection	n	T_0 (GeV)	a_0	$\langle \beta_t \rangle$ (c)	χ^2/ndof	
Figure 7(a)	π^-	62.4	0-5%	8.9 ± 0.2	0.183 ± 0.003	-0.419 ± 0.005	0.125 ± 0.003	82/5	
			$ y < 0.1$	5-10%	8.3 ± 0.2	0.175 ± 0.003	-0.416 ± 0.005	0.123 ± 0.003	83/5
				10-20%	7.8 ± 0.2	0.171 ± 0.003	-0.414 ± 0.005	0.122 ± 0.003	73/5
				20-30%	7.5 ± 0.2	0.168 ± 0.003	-0.412 ± 0.005	0.121 ± 0.003	69/5
				30-40%	6.7 ± 0.1	0.162 ± 0.003	-0.410 ± 0.005	0.119 ± 0.003	62/5
				40-50%	6.4 ± 0.1	0.159 ± 0.003	-0.408 ± 0.005	0.118 ± 0.003	29/5
				50-60%	6.0 ± 0.1	0.154 ± 0.003	-0.404 ± 0.005	0.115 ± 0.003	29/5
				60-70%	5.7 ± 0.1	0.146 ± 0.002	-0.394 ± 0.005	0.111 ± 0.003	20/5
				70-80%	5.5 ± 0.1	0.139 ± 0.002	-0.388 ± 0.005	0.106 ± 0.003	4/5
Figure 7(b)	π^+	62.4	0-5%	8.2 ± 0.2	0.195 ± 0.003	-0.426 ± 0.005	0.130 ± 0.003	65/5	
			$ y < 0.1$	5-10%	7.5 ± 0.2	0.188 ± 0.003	-0.424 ± 0.005	0.126 ± 0.003	103/5
				10-20%	6.6 ± 0.1	0.178 ± 0.003	-0.422 ± 0.005	0.125 ± 0.003	71/5
				20-30%	6.3 ± 0.1	0.172 ± 0.003	-0.420 ± 0.005	0.124 ± 0.003	84/5
				30-40%	6.1 ± 0.1	0.168 ± 0.003	-0.418 ± 0.005	0.123 ± 0.003	52/5
				40-50%	6.0 ± 0.1	0.161 ± 0.003	-0.414 ± 0.005	0.121 ± 0.003	31/5
				50-60%	5.8 ± 0.1	0.154 ± 0.003	-0.411 ± 0.005	0.118 ± 0.003	29/5
				60-70%	5.6 ± 0.1	0.147 ± 0.002	-0.407 ± 0.005	0.115 ± 0.003	20/5
				70-80%	5.6 ± 0.1	0.140 ± 0.002	-0.405 ± 0.005	0.113 ± 0.003	7/5
Figure 7(c)	K^-	62.4	0-5%	15.8 ± 0.6	0.178 ± 0.003	-0.038 ± 0.005	0.193 ± 0.005	21/5	
			$ y < 0.1$	5-10%	13.1 ± 0.4	0.173 ± 0.003	-0.026 ± 0.004	0.184 ± 0.005	4/5
				10-20%	12.3 ± 0.3	0.170 ± 0.003	-0.018 ± 0.004	0.175 ± 0.005	8/5
				20-30%	11.3 ± 0.3	0.166 ± 0.003	-0.009 ± 0.004	0.166 ± 0.005	4/5
				30-40%	10.2 ± 0.3	0.157 ± 0.003	-0.007 ± 0.004	0.159 ± 0.005	5/5
				40-50%	9.7 ± 0.2	0.144 ± 0.002	-0.022 ± 0.004	0.152 ± 0.005	12/5
				50-60%	9.4 ± 0.2	0.136 ± 0.002	-0.015 ± 0.004	0.143 ± 0.005	7/5
				60-70%	8.5 ± 0.2	0.127 ± 0.002	-0.008 ± 0.004	0.129 ± 0.005	7/5
				70-80%	7.1 ± 0.2	0.119 ± 0.002	0.004 ± 0.004	0.119 ± 0.005	9/5
Figure 7(d)	K^+	62.4	0-5%	18.1 ± 0.8	0.180 ± 0.003	-0.052 ± 0.005	0.171 ± 0.005	11/5	
			$ y < 0.1$	5-10%	14.2 ± 0.5	0.177 ± 0.003	-0.039 ± 0.005	0.163 ± 0.005	9/5
				10-20%	11.1 ± 0.3	0.171 ± 0.003	-0.030 ± 0.005	0.157 ± 0.005	8/5
				20-30%	9.2 ± 0.2	0.166 ± 0.003	-0.027 ± 0.004	0.149 ± 0.005	5/5
				30-40%	7.4 ± 0.2	0.158 ± 0.003	-0.022 ± 0.004	0.142 ± 0.005	2/5
				40-50%	7.3 ± 0.2	0.148 ± 0.002	-0.017 ± 0.004	0.137 ± 0.005	4/5
				50-60%	6.7 ± 0.1	0.140 ± 0.002	-0.016 ± 0.004	0.132 ± 0.005	9/5
				60-70%	5.9 ± 0.1	0.135 ± 0.002	-0.016 ± 0.004	0.129 ± 0.005	3/5
				70-80%	5.4 ± 0.1	0.123 ± 0.002	-0.012 ± 0.004	0.125 ± 0.005	8/5
Figure 7(e)	\bar{p}	62.4	0-5%	12.6 ± 0.3	0.142 ± 0.002	-0.004 ± 0.004	0.428 ± 0.008	94/11	
			$ y < 0.1$	5-10%	12.3 ± 0.3	0.138 ± 0.002	0.001 ± 0.004	0.424 ± 0.008	105/11
				10-20%	11.4 ± 0.3	0.133 ± 0.002	0.003 ± 0.004	0.410 ± 0.008	81/11
				20-30%	10.0 ± 0.3	0.129 ± 0.002	0.003 ± 0.004	0.392 ± 0.008	114/11
				30-40%	10.7 ± 0.3	0.121 ± 0.002	0.007 ± 0.004	0.375 ± 0.008	96/11
				40-50%	9.2 ± 0.2	0.112 ± 0.002	0.009 ± 0.004	0.349 ± 0.008	76/11
				50-60%	8.9 ± 0.2	0.106 ± 0.002	0.011 ± 0.004	0.320 ± 0.008	50/11
				60-70%	8.1 ± 0.2	0.096 ± 0.002	0.014 ± 0.004	0.317 ± 0.008	75/11
				70-80%	7.8 ± 0.2	0.090 ± 0.002	0.015 ± 0.004	0.303 ± 0.008	99/11
Figure 7(f)	p	62.4	0-5%	12.7 ± 0.3	0.148 ± 0.002	-0.009 ± 0.004	0.395 ± 0.008	29/10	
			$ y < 0.1$	5-10%	12.5 ± 0.3	0.148 ± 0.002	-0.005 ± 0.004	0.390 ± 0.008	14/10
				10-20%	10.8 ± 0.3	0.142 ± 0.002	-0.001 ± 0.004	0.381 ± 0.008	20/10
				20-30%	11.0 ± 0.3	0.138 ± 0.002	0.004 ± 0.004	0.372 ± 0.008	18/10
				30-40%	11.1 ± 0.3	0.136 ± 0.002	0.005 ± 0.004	0.363 ± 0.008	10/10
				40-50%	10.2 ± 0.3	0.129 ± 0.002	0.008 ± 0.004	0.350 ± 0.008	12/10
				50-60%	9.9 ± 0.2	0.117 ± 0.002	0.009 ± 0.004	0.344 ± 0.008	9/10
				60-70%	9.2 ± 0.2	0.108 ± 0.002	0.010 ± 0.004	0.321 ± 0.008	9/10
				70-80%	8.3 ± 0.2	0.100 ± 0.002	0.010 ± 0.004	0.301 ± 0.008	9/10

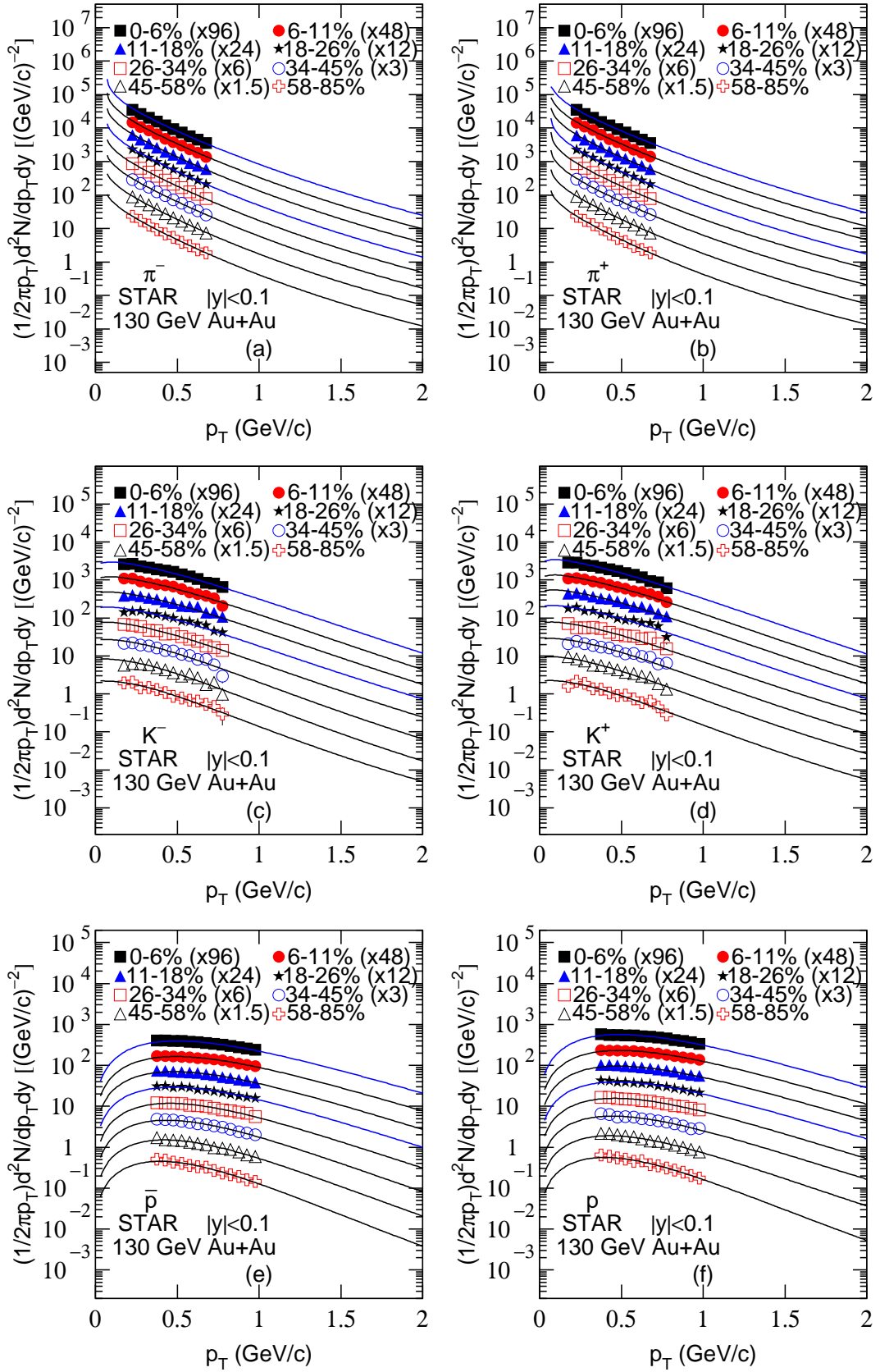


Figure 8. Same as Figure 1, but showing the results for 130 GeV Au-Au collisions with another set of centrality intervals. The symbols represent the STAR data [35].

Table 8. Values of n , T_0 , a_0 , $\langle\beta_t\rangle$, χ^2 , and ndof corresponding to the curves in Figure 8.

Figure	Particle	$\sqrt{s_{NN}}$ (GeV)	Selection	n	T_0 (GeV)	a_0	$\langle\beta_t\rangle$ (c)	χ^2/ndof	
Figure 8(a)	π^-	130	0–6%	7.2 ± 0.2	0.185 ± 0.003	-0.435 ± 0.005	0.131 ± 0.003	54/5	
			$ y < 0.1$	6–11%	6.8 ± 0.1	0.177 ± 0.003	-0.432 ± 0.005	0.124 ± 0.003	46/5
			11–18%	6.6 ± 0.1	0.173 ± 0.003	-0.431 ± 0.005	0.122 ± 0.003	34/5	
			18–26%	6.4 ± 0.1	0.170 ± 0.003	-0.430 ± 0.005	0.121 ± 0.003	17/5	
			26–34%	6.2 ± 0.1	0.165 ± 0.003	-0.427 ± 0.005	0.119 ± 0.003	12/5	
			34–45%	6.1 ± 0.1	0.163 ± 0.003	-0.426 ± 0.005	0.118 ± 0.003	14/5	
			45–58%	5.5 ± 0.1	0.157 ± 0.003	-0.424 ± 0.005	0.115 ± 0.003	9/5	
			58–85%	5.3 ± 0.1	0.150 ± 0.003	-0.414 ± 0.005	0.113 ± 0.003	8/5	
Figure 8(b)	π^+	130	0–6%	8.0 ± 0.2	0.198 ± 0.003	-0.429 ± 0.005	0.137 ± 0.003	14/5	
			$ y < 0.1$	6–11%	7.3 ± 0.2	0.191 ± 0.003	-0.427 ± 0.005	0.134 ± 0.003	13/5
			11–18%	6.4 ± 0.1	0.181 ± 0.003	-0.424 ± 0.005	0.132 ± 0.003	14/5	
			18–26%	6.1 ± 0.1	0.177 ± 0.003	-0.417 ± 0.005	0.130 ± 0.003	18/5	
			26–34%	5.7 ± 0.1	0.174 ± 0.003	-0.416 ± 0.005	0.126 ± 0.003	13/5	
			34–45%	5.4 ± 0.1	0.164 ± 0.003	-0.413 ± 0.005	0.125 ± 0.003	9/5	
			45–58%	5.4 ± 0.1	0.159 ± 0.003	-0.411 ± 0.005	0.124 ± 0.003	15/5	
			58–85%	5.0 ± 0.1	0.150 ± 0.003	-0.410 ± 0.005	0.123 ± 0.003	18/5	
Figure 8(c)	K^-	130	0–6%	14.3 ± 0.5	0.183 ± 0.003	-0.038 ± 0.005	0.209 ± 0.005	7/8	
			$ y < 0.1$	6–11%	12.9 ± 0.3	0.177 ± 0.003	-0.027 ± 0.004	0.196 ± 0.005	9/8
			11–18%	10.8 ± 0.3	0.174 ± 0.003	-0.019 ± 0.004	0.181 ± 0.005	5/8	
			18–26%	8.3 ± 0.2	0.168 ± 0.003	-0.016 ± 0.004	0.167 ± 0.005	12/8	
			26–34%	8.0 ± 0.2	0.161 ± 0.003	-0.014 ± 0.004	0.159 ± 0.005	7/8	
			34–45%	7.6 ± 0.2	0.148 ± 0.002	-0.007 ± 0.004	0.154 ± 0.005	10/8	
			45–58%	7.1 ± 0.2	0.141 ± 0.002	-0.003 ± 0.004	0.144 ± 0.005	14/8	
			58–85%	5.6 ± 0.1	0.132 ± 0.002	0.001 ± 0.004	0.137 ± 0.005	7/8	
Figure 8(d)	K^+	130	0–6%	15.9 ± 0.6	0.186 ± 0.003	-0.054 ± 0.005	0.194 ± 0.005	10/8	
			$ y < 0.1$	6–11%	14.1 ± 0.5	0.181 ± 0.003	-0.041 ± 0.005	0.188 ± 0.005	10/8
			11–18%	11.2 ± 0.3	0.175 ± 0.003	-0.032 ± 0.005	0.182 ± 0.005	7/8	
			18–26%	9.3 ± 0.2	0.170 ± 0.003	-0.022 ± 0.004	0.171 ± 0.005	12/8	
			26–34%	7.6 ± 0.2	0.163 ± 0.003	-0.017 ± 0.004	0.167 ± 0.005	17/8	
			34–45%	6.9 ± 0.1	0.152 ± 0.003	-0.013 ± 0.004	0.162 ± 0.005	15/8	
			45–58%	6.3 ± 0.1	0.144 ± 0.002	-0.011 ± 0.004	0.159 ± 0.005	7/8	
			58–85%	5.9 ± 0.1	0.138 ± 0.002	-0.009 ± 0.004	0.147 ± 0.005	15/8	
Figure 8(e)	\bar{p}	130	0–6%	12.1 ± 0.3	0.146 ± 0.002	-0.006 ± 0.004	0.457 ± 0.008	81/8	
			$ y < 0.1$	6–11%	11.9 ± 0.3	0.143 ± 0.002	-0.002 ± 0.004	0.444 ± 0.008	33/8
			11–18%	11.3 ± 0.3	0.137 ± 0.002	0.002 ± 0.004	0.429 ± 0.008	12/8	
			18–26%	10.7 ± 0.3	0.133 ± 0.002	0.003 ± 0.004	0.421 ± 0.008	32/8	
			26–34%	9.3 ± 0.2	0.125 ± 0.002	0.007 ± 0.004	0.398 ± 0.008	25/8	
			34–45%	9.0 ± 0.2	0.117 ± 0.002	0.008 ± 0.004	0.375 ± 0.008	26/8	
			45–58%	8.7 ± 0.2	0.110 ± 0.002	0.011 ± 0.004	0.367 ± 0.008	25/8	
			58–85%	7.9 ± 0.2	0.102 ± 0.002	0.012 ± 0.004	0.328 ± 0.008	22/8	
Figure 8(f)	p	130	0–6%	12.3 ± 0.4	0.149 ± 0.002	-0.009 ± 0.004	0.439 ± 0.008	66/8	
			$ y < 0.1$	6–11%	12.0 ± 0.4	0.148 ± 0.002	-0.006 ± 0.004	0.432 ± 0.008	41/8
			11–18%	10.6 ± 0.3	0.144 ± 0.002	-0.002 ± 0.004	0.425 ± 0.008	13/8	
			18–26%	9.2 ± 0.2	0.139 ± 0.002	0.001 ± 0.004	0.411 ± 0.008	6/8	
			26–34%	8.9 ± 0.2	0.133 ± 0.002	0.004 ± 0.004	0.398 ± 0.008	16/8	
			34–45%	8.1 ± 0.2	0.129 ± 0.002	0.007 ± 0.004	0.375 ± 0.008	24/8	
			45–58%	7.7 ± 0.2	0.117 ± 0.002	0.008 ± 0.004	0.363 ± 0.008	10/8	
58–85%	7.4 ± 0.2	0.102 ± 0.002	0.010 ± 0.004	0.333 ± 0.008	11/8				

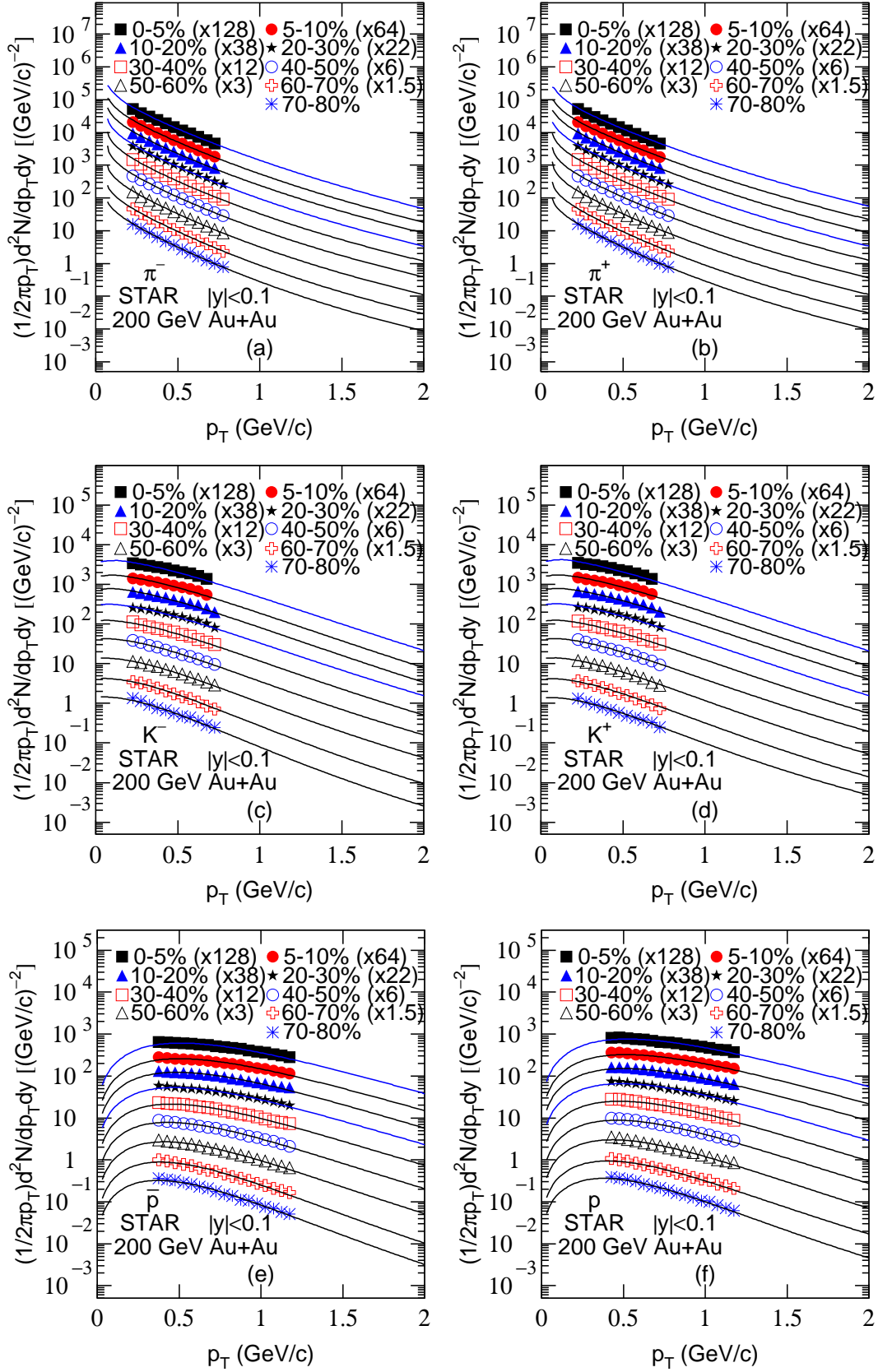


Figure 9. Same as Figure 1, but showing the results for 200 GeV Au+Au collisions. The symbols represent the STAR data [35].

Table 9. Values of n , T_0 , a_0 , $\langle\beta_t\rangle$, χ^2 , and ndof corresponding to the curves in Figure 9.

Figure	Particle	$\sqrt{s_{NN}}$ (GeV)	Selection	n	T_0 (GeV)	a_0	$\langle\beta_t\rangle$ (c)	χ^2/ndof	
Figure 9(a)	π^-	200	0–5%	6.7 ± 0.1	0.189 ± 0.003	-0.439 ± 0.005	0.139 ± 0.003	58/6	
			$ y < 0.1$	5–10%	6.1 ± 0.1	0.180 ± 0.003	-0.437 ± 0.005	0.138 ± 0.003	50/6
				10–20%	5.7 ± 0.1	0.178 ± 0.003	-0.434 ± 0.005	0.135 ± 0.003	77/6
				20–30%	5.5 ± 0.1	0.174 ± 0.003	-0.432 ± 0.005	0.133 ± 0.003	64/7
				30–40%	5.2 ± 0.1	0.168 ± 0.003	-0.430 ± 0.005	0.132 ± 0.003	54/7
				40–50%	5.1 ± 0.1	0.167 ± 0.003	-0.426 ± 0.005	0.125 ± 0.003	46/7
				50–60%	5.0 ± 0.1	0.160 ± 0.003	-0.423 ± 0.005	0.123 ± 0.003	33/7
				60–70%	5.0 ± 0.1	0.153 ± 0.003	-0.420 ± 0.005	0.120 ± 0.003	13/7
				70–80%	4.9 ± 0.1	0.145 ± 0.002	-0.419 ± 0.005	0.116 ± 0.003	5/7
Figure 9(b)	π^+	200	0–5%	7.0 ± 0.1	0.201 ± 0.003	-0.432 ± 0.005	0.141 ± 0.003	29/6	
			$ y < 0.1$	5–10%	6.4 ± 0.1	0.194 ± 0.003	-0.426 ± 0.005	0.139 ± 0.003	24/6
				10–20%	6.3 ± 0.1	0.184 ± 0.003	-0.421 ± 0.005	0.137 ± 0.003	42/6
				20–30%	6.1 ± 0.1	0.180 ± 0.003	-0.418 ± 0.005	0.135 ± 0.003	25/7
				30–40%	5.7 ± 0.1	0.177 ± 0.003	-0.416 ± 0.005	0.132 ± 0.003	16/7
				40–50%	5.5 ± 0.1	0.167 ± 0.003	-0.412 ± 0.005	0.131 ± 0.003	31/7
				50–60%	5.2 ± 0.1	0.162 ± 0.003	-0.406 ± 0.005	0.130 ± 0.003	26/7
				60–70%	4.9 ± 0.1	0.153 ± 0.003	-0.403 ± 0.005	0.125 ± 0.003	11/7
				70–80%	4.8 ± 0.1	0.146 ± 0.002	-0.401 ± 0.005	0.124 ± 0.003	2/7
Figure 9(c)	K^-	200	0–5%	12.4 ± 0.3	0.187 ± 0.003	-0.040 ± 0.005	0.232 ± 0.005	9/5	
			$ y < 0.1$	5–10%	11.3 ± 0.3	0.181 ± 0.003	-0.033 ± 0.005	0.212 ± 0.005	8/5
				10–20%	10.4 ± 0.3	0.178 ± 0.003	-0.026 ± 0.004	0.195 ± 0.005	8/6
				20–30%	7.9 ± 0.2	0.174 ± 0.003	-0.018 ± 0.004	0.183 ± 0.005	8/6
				30–40%	7.4 ± 0.2	0.165 ± 0.003	-0.015 ± 0.004	0.173 ± 0.005	5/6
				40–50%	6.0 ± 0.1	0.152 ± 0.003	-0.010 ± 0.004	0.162 ± 0.005	5/6
				50–60%	5.9 ± 0.1	0.145 ± 0.002	-0.007 ± 0.004	0.150 ± 0.005	4/6
				60–70%	5.9 ± 0.1	0.136 ± 0.002	-0.004 ± 0.004	0.136 ± 0.005	4/6
				70–80%	5.6 ± 0.1	0.127 ± 0.002	-0.003 ± 0.004	0.128 ± 0.005	12/6
Figure 9(d)	K^+	200	0–5%	13.9 ± 0.3	0.188 ± 0.003	-0.053 ± 0.005	0.239 ± 0.005	10/5	
			$ y < 0.1$	5–10%	11.6 ± 0.3	0.183 ± 0.003	-0.039 ± 0.005	0.227 ± 0.005	8/5
				10–20%	9.6 ± 0.2	0.178 ± 0.003	-0.030 ± 0.005	0.217 ± 0.005	6/6
				20–30%	8.7 ± 0.2	0.173 ± 0.003	-0.026 ± 0.004	0.208 ± 0.005	5/6
				30–40%	7.7 ± 0.2	0.166 ± 0.003	-0.020 ± 0.004	0.197 ± 0.005	4/6
				40–50%	6.0 ± 0.1	0.156 ± 0.003	-0.017 ± 0.004	0.187 ± 0.005	4/6
				50–60%	5.8 ± 0.1	0.148 ± 0.002	-0.014 ± 0.004	0.176 ± 0.005	3/6
				60–70%	5.5 ± 0.1	0.143 ± 0.002	-0.012 ± 0.004	0.162 ± 0.005	5/6
				70–80%	4.4 ± 0.1	0.131 ± 0.002	-0.007 ± 0.004	0.155 ± 0.005	6/6
Figure 9(e)	\bar{p}	200	0–5%	11.8 ± 0.3	0.151 ± 0.003	-0.012 ± 0.004	0.472 ± 0.008	79/12	
			$ y < 0.1$	5–10%	10.5 ± 0.3	0.147 ± 0.002	-0.011 ± 0.004	0.464 ± 0.008	89/12
				10–20%	10.3 ± 0.3	0.141 ± 0.002	-0.010 ± 0.004	0.446 ± 0.008	80/12
				20–30%	8.4 ± 0.2	0.138 ± 0.002	-0.010 ± 0.004	0.428 ± 0.008	89/12
				30–40%	6.8 ± 0.1	0.129 ± 0.002	-0.009 ± 0.004	0.399 ± 0.008	57/12
				40–50%	6.3 ± 0.1	0.121 ± 0.002	-0.007 ± 0.004	0.374 ± 0.008	74/12
				50–60%	6.2 ± 0.1	0.115 ± 0.002	-0.005 ± 0.004	0.347 ± 0.008	44/12
				60–70%	5.9 ± 0.1	0.104 ± 0.002	-0.005 ± 0.004	0.317 ± 0.008	69/12
				70–80%	5.8 ± 0.1	0.103 ± 0.002	-0.002 ± 0.004	0.289 ± 0.007	43/12
Figure 9(f)	p	200	0–5%	11.7 ± 0.3	0.154 ± 0.003	-0.011 ± 0.004	0.492 ± 0.008	30/11	
			$ y < 0.1$	5–10%	11.2 ± 0.3	0.151 ± 0.003	-0.008 ± 0.004	0.478 ± 0.008	35/11
				10–20%	10.8 ± 0.3	0.145 ± 0.002	-0.005 ± 0.004	0.466 ± 0.008	23/11
				20–30%	8.8 ± 0.2	0.133 ± 0.002	0.002 ± 0.004	0.449 ± 0.008	31/11
				30–40%	8.1 ± 0.2	0.127 ± 0.002	0.003 ± 0.004	0.436 ± 0.008	29/11
				40–50%	7.5 ± 0.2	0.122 ± 0.002	0.004 ± 0.004	0.417 ± 0.008	30/11
				50–60%	6.8 ± 0.1	0.118 ± 0.002	0.006 ± 0.004	0.371 ± 0.008	44/11
				60–70%	5.3 ± 0.1	0.107 ± 0.002	0.008 ± 0.004	0.338 ± 0.008	36/11
				70–80%	5.1 ± 0.1	0.103 ± 0.002	0.008 ± 0.004	0.338 ± 0.008	36/11

B. Tendencies of parameters

We now analyze the tendencies of parameters on collision energy $\sqrt{s_{NN}}$ and centrality interval (percentage). In Figure 11, the dependence of parameter n on $\sqrt{s_{NN}}$ and centrality is shown, where panels (a)–(f) are for the results from the spectra of π^- , π^+ , K^- , K^+ , \bar{p} , and p , respectively. It is not difficult to find out that with the increase of $\sqrt{s_{NN}}$, the values of n decrease significantly. Meanwhile, with the decrease of centrality from central to peripheral collisions, the values of n also decrease. As we know, n is used to describe the degree of non-equilibrium of the system. The larger the value of n is, the closer to equilibrium the system is. This work shows that the system at lower energy and in central collisions corresponds to larger n and hence to higher degree of equilibrium, compared with the system at higher energy and in peripheral collisions.

As one of the core concepts in thermodynamics and statistical mechanics, temperature is also the attention of our research. Generally, we can directly extract the temperature information of the system from particle spectra. Panels (a)–(f) in Figure 12 show the dependence of thermal freeze-out temperature T_0 on $\sqrt{s_{NN}}$ extracted from the spectra of six kinds of charged hadrons in different centrality intervals. It can be clearly seen that in the available central collisions, T_0 increases rapidly in $\sqrt{s_{NN}} = 2.7\text{--}7.7$ GeV range. When $\sqrt{s_{NN}}$ is larger than 7.7 GeV, T_0 increases slowly. The higher the temperature is, the higher the excitation degree is. As $\sqrt{s_{NN}}$ increases, the excitation degree of the system also increases. The change trend of T_0 with $\sqrt{s_{NN}}$ can well reflect this change phenomenon of the excitation degree. At nine collision energies and for six kinds of particles, T_0 decreases with the decrease of the centrality from central to peripheral collisions.

Similar to Figures 11 and 12, the dependence of the dimensionless correction index a_0 on $\sqrt{s_{NN}}$ is shown in Figures 13(a)–13(f) for different centrality intervals and charged hadrons. From Figure 13 one can see that with the increase of $\sqrt{s_{NN}}$, in the available central collisions, a_0 increases quickly and then decreases significantly, and the boundary energy is 7.7 GeV. The values of a_0 from π^\mp spectra are negative, which is significantly less than those from K^\mp and $\bar{p}(p)$ spectra. From central to peripheral collisions, a_0 increases significantly for different kinds of

particles in the available energy range.

Figure 14 demonstrates the relationship between the average transverse flow velocity $\langle\beta_t\rangle$ and $\sqrt{s_{NN}}$ for different particles in panels (a)–(f), where the results for different centrality intervals are shown. With increasing $\sqrt{s_{NN}}$, one can see a significantly increasing $\langle\beta_t\rangle$ for different hadrons in most cases. At different energies, $\langle\beta_t\rangle$ for each kind of particles from central to peripheral collisions decreases gradually. Observing the values of $\langle\beta_t\rangle$, one can clearly find that the order of flow velocity is $\bar{p}(p) > K^\mp > \pi^\mp$.

In order to represent the chaos degree of the final state particle information, we show the dependence of pseudo-entropy S'_{hadron} on $\sqrt{s_{NN}}$ and centrality in Figure 15, where panels (a)–(f) are orderly for the results of π^- , π^+ , K^- , K^+ , \bar{p} , and p . One can see that S'_{hadron} of the six kinds of hadrons in different centrality intervals increases with the increase of $\sqrt{s_{NN}}$. In particular, for π^\mp and K^\mp and in central collisions, S'_{hadron} increases quickly and then slowly with the increase of $\sqrt{s_{NN}}$, and the boundary energy is 7.7 GeV. From central to peripheral collisions, S'_{hadron} decreases gradually. The chaos degree of particle information at low energy is less than that at high energy. In addition, the chaos degree in central collisions is larger than that in peripheral collisions. Observing the values of S'_{hadron} , one can clearly find that the order of chaos degree is $\bar{p}(p) > K^\mp > \pi^\mp$.

In the above discussion, we have used a particular parameterization for the p_T distribution and obtained the tendencies of parameters, but many other parameterizations are available and used in the field. Our conclusions on the behaviors of main parameters n [or $q = (n+1)/n$], T_0 , and $\langle\beta_t\rangle$ with increasing the collision energy, event centrality, and particle mass are similar to others if one uses different parameterizations [48], though the absolute sizes may be different. The parameter a_0 is a new one introduced by us recently [45], which is hard to compare with others at present due to the lack of related work, though the relative sizes of a_0 on particle mass are understandable. The parameterization used in this paper is also suitable for smaller system studied in our previous work [45, 46], where the dependences of parameters on the collision energy, event centrality (or multiplicity), and particle mass are similar, which is not very sensitive to the system size.

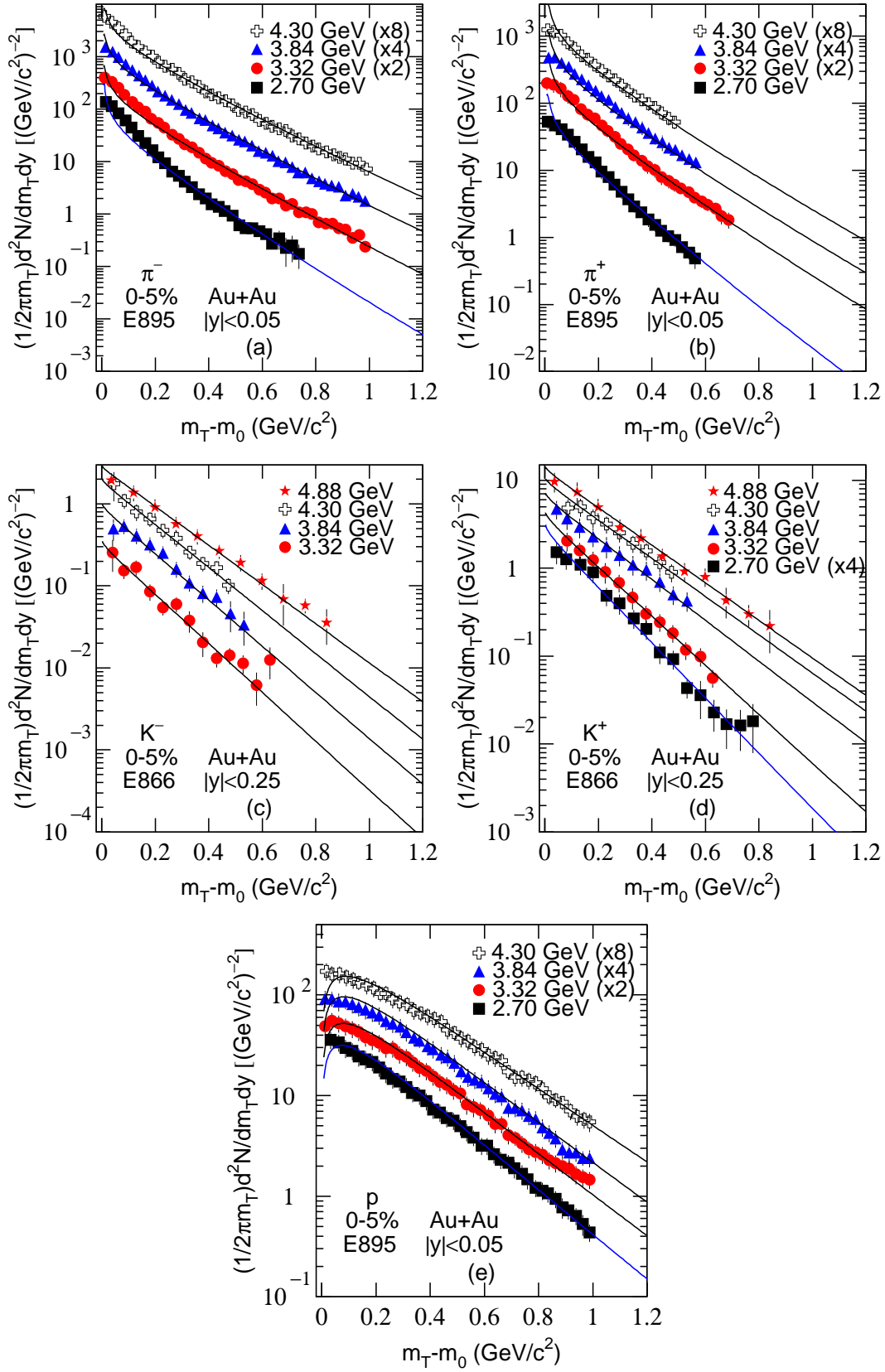


Figure 10. Transverse mass spectra of π^- (a), π^+ (b), K^- (c), K^+ (d), and p (e) produced in 0-5% Au-Au collisions at mid-rapidity at $\sqrt{s_{NN}} = 2.70, 3.32, 3.84, 4.30,$ and 4.88 GeV, where only panel (d) contains five energies. The symbols in panels (a), (b), and (e) represent the experimental data measured by the E895 Collaboration [36], and those in panels (c) and (d) are from the E866 Collaboration [37], where some sets of data are re-scaled by different amounts. The data for \bar{p} is not available in the same or similar experiments. The curves are our results fitted by Eq. (4) for π^\pm and K^\pm [panels (a)–(d)] or Eq. (6) for p [panel (e)].

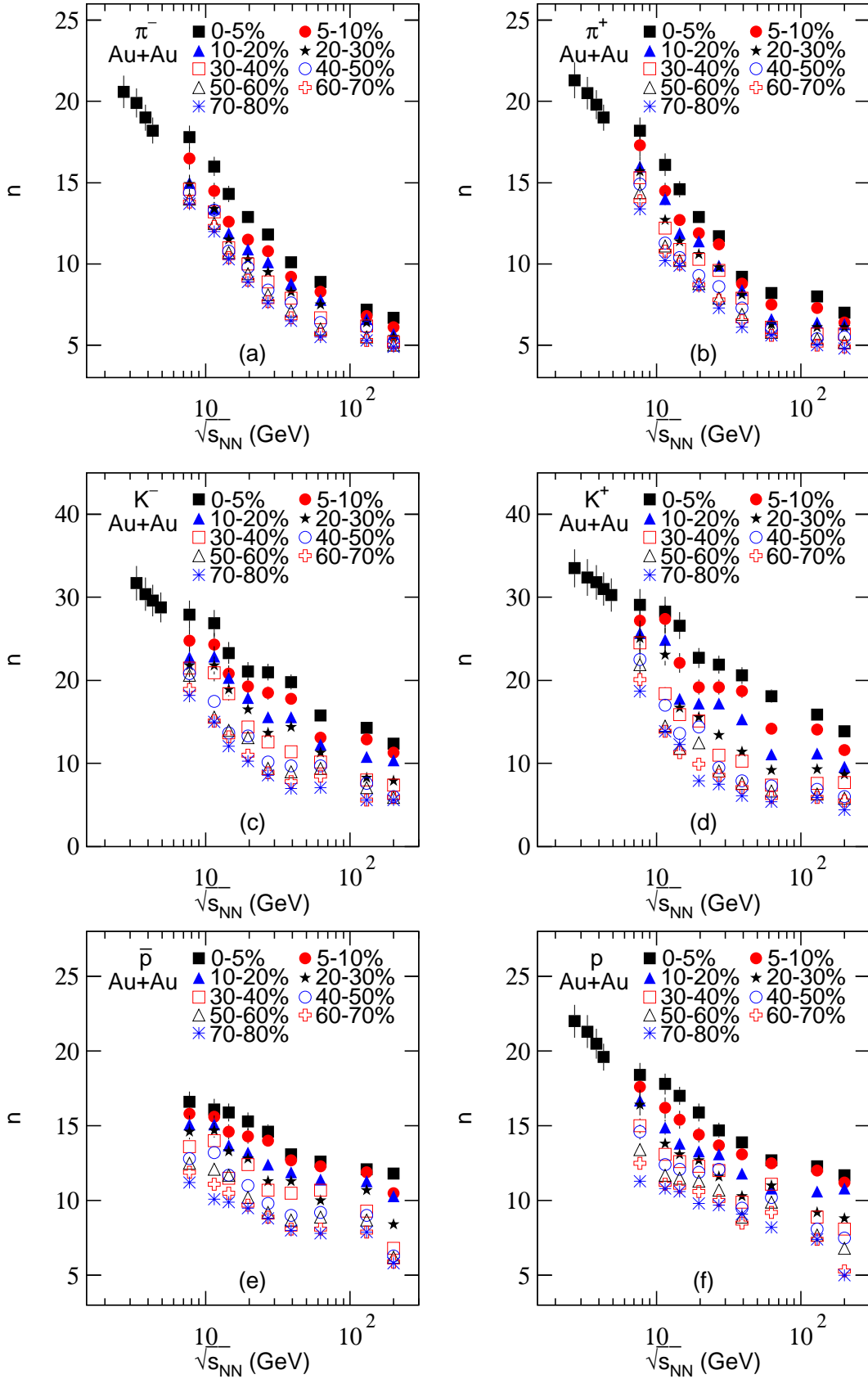


Figure 11. Dependence of power index n on collision energy $\sqrt{s_{NN}}$ in Au-Au collision with nine main centrality intervals which are marked in the panels. Figures 11(a)–11(f) correspond to the results from π^- , π^+ , K^- , K^+ , \bar{p} , and p spectra, respectively. In particular, at 130 GeV, the centrality intervals 0–6%, 6–11%, 11–18%, 18–26%, 26–34%, 34–45%, and 45–58% are orderly classified into the closest main centrality intervals, and the centrality interval 58–85% is simultaneously classified into 60–70% and 70–80%. The results for different particles are cited from Tables 1–10.

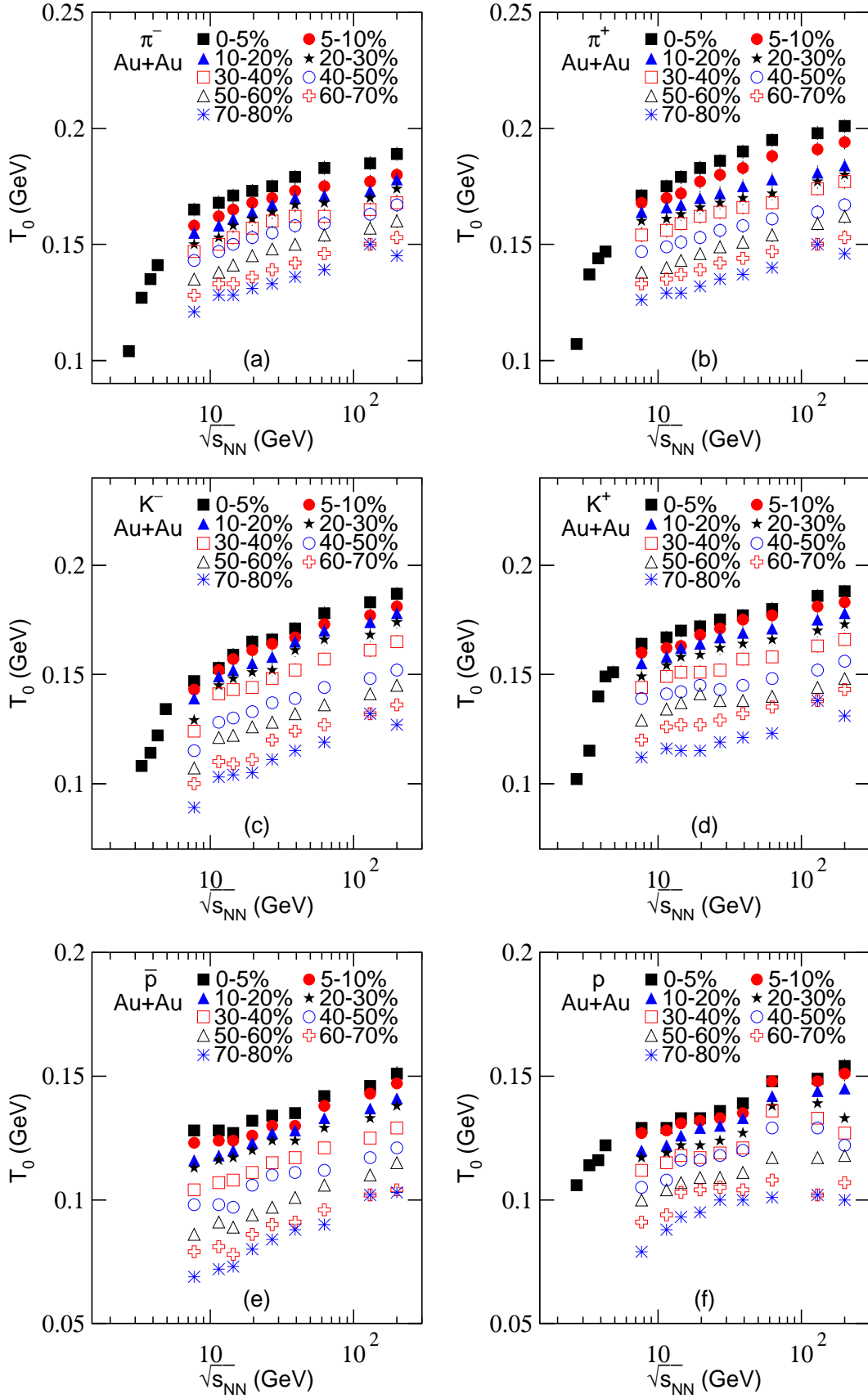


Figure 12. Same as Figure 11, but showing the dependence of thermal freeze-out temperature T_0 on $\sqrt{s_{NN}}$.

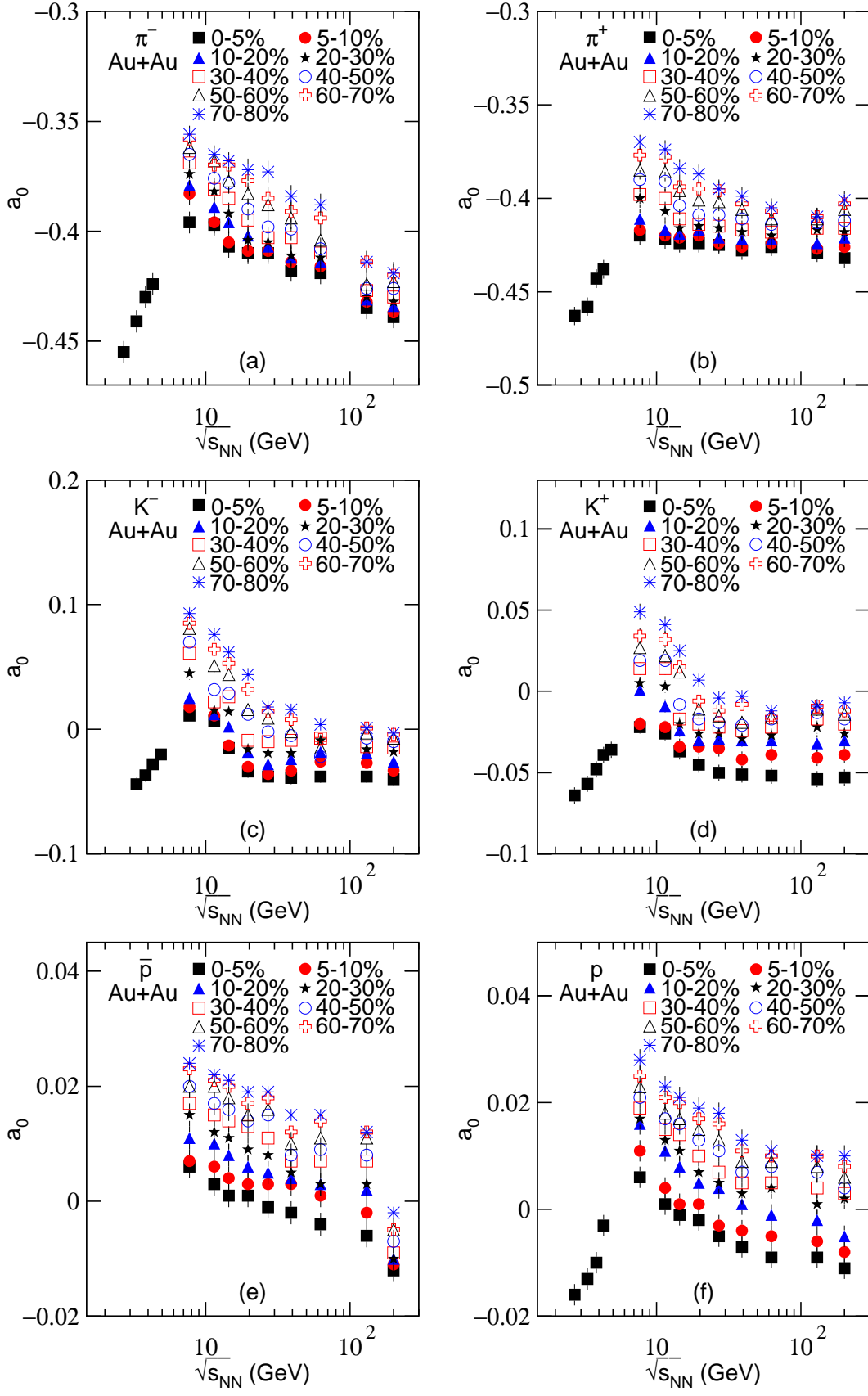


Figure 13. Same as Figure 11, but showing the dependence of correction index a_0 on $\sqrt{s_{NN}}$.

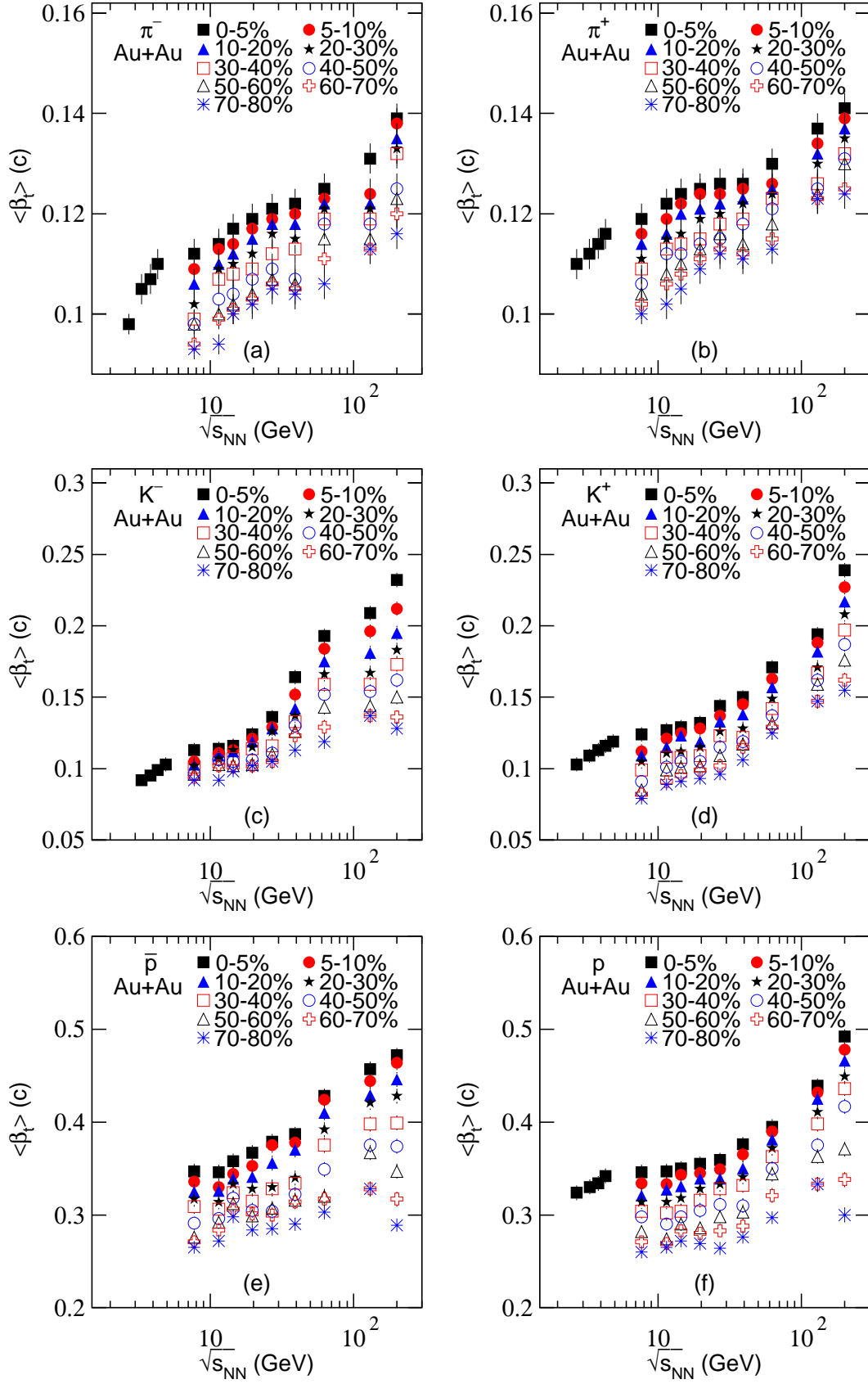


Figure 14. Same as Figure 11, but showing the dependence of average transverse flow velocity $\langle \beta_t \rangle$ on $\sqrt{s_{NN}}$.

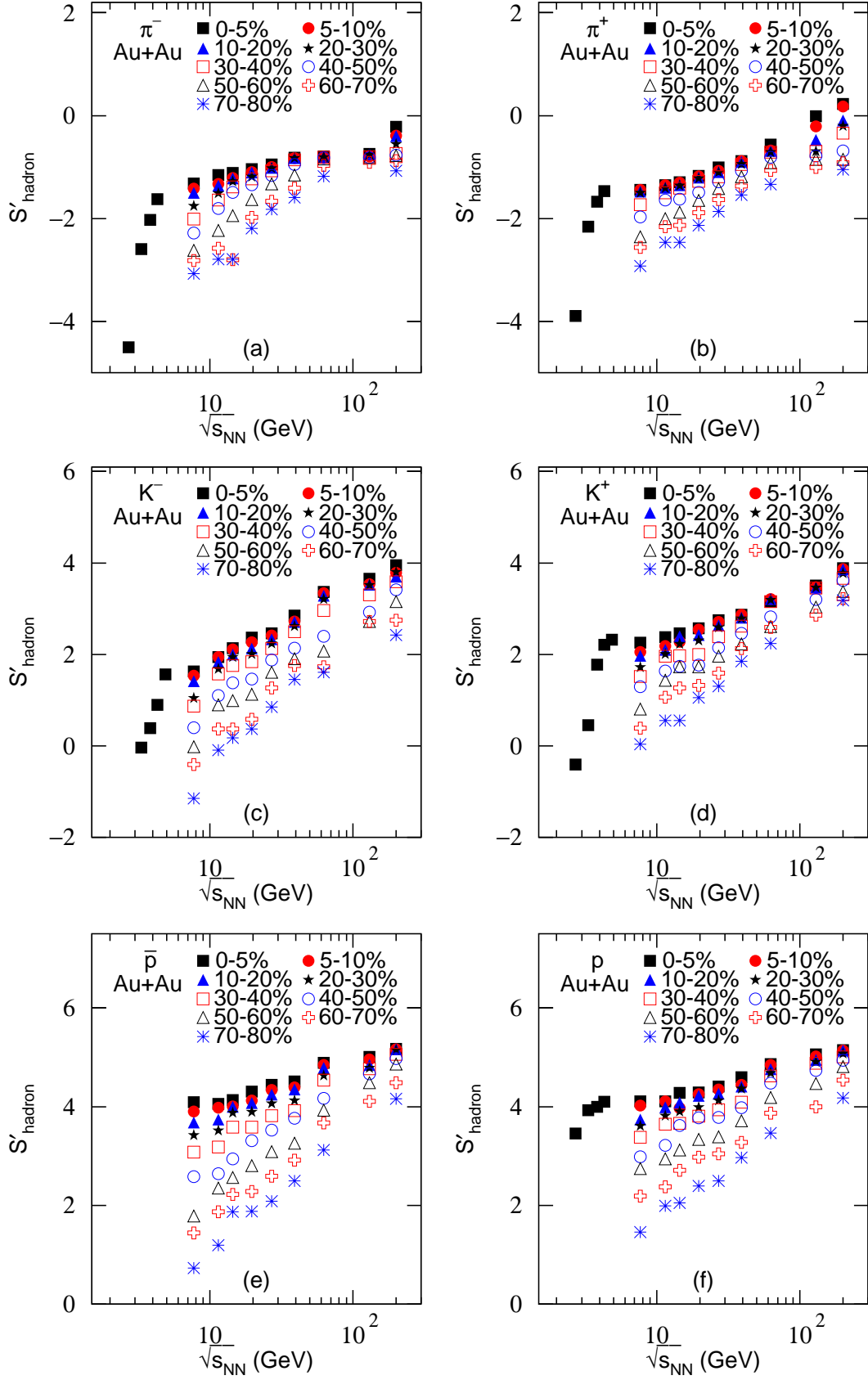


Figure 15. Same as Figures 11 and 15, but showing the dependence of pseudo-entropy S'_{hadron} on C .

Table 10. Values of n , T_0 , a_0 , $\langle\beta_t\rangle$, χ^2 , and ndof corresponding to the curves in Figure 10.

Figure	Particle	$\sqrt{s_{NN}}$ (GeV)	Selection	n	T_0 (GeV)	a_0	$\langle\beta_t\rangle$ (c)	χ^2/ndof
Figure 10(a)	π^-	2.70	0–5%	20.6 ± 1.0	0.104 ± 0.002	-0.455 ± 0.005	0.098 ± 0.002	35/25
		3.32	$ y < 0.05$	19.9 ± 0.9	0.127 ± 0.002	-0.441 ± 0.005	0.105 ± 0.003	30/35
		3.84		19.0 ± 0.8	0.135 ± 0.002	-0.430 ± 0.005	0.107 ± 0.003	13/35
		4.30		18.2 ± 0.8	0.141 ± 0.002	-0.424 ± 0.005	0.110 ± 0.003	13/35
Figure 10(b)	π^+	2.70	0–5%	21.3 ± 1.1	0.107 ± 0.002	-0.463 ± 0.005	0.110 ± 0.003	53/18
		3.32	$ y < 0.05$	20.5 ± 1.0	0.137 ± 0.002	-0.458 ± 0.005	0.112 ± 0.003	56/23
		3.84		19.8 ± 0.9	0.144 ± 0.002	-0.443 ± 0.005	0.114 ± 0.003	54/18
		4.30		19.0 ± 0.8	0.147 ± 0.002	-0.438 ± 0.005	0.116 ± 0.003	61/15
Figure 10(c)	K^-	3.32	0–5%	31.7 ± 2.1	0.108 ± 0.002	-0.044 ± 0.005	0.092 ± 0.004	9/8
		3.84	$ y < 0.25$	30.4 ± 2.0	0.114 ± 0.002	-0.037 ± 0.005	0.095 ± 0.004	4/6
		4.30		29.6 ± 1.9	0.122 ± 0.002	-0.028 ± 0.004	0.099 ± 0.004	1/5
		4.88		28.8 ± 1.8	0.134 ± 0.002	-0.020 ± 0.004	0.103 ± 0.005	1/6
Figure 10(d)	K^+	2.70	0–5%	33.5 ± 2.3	0.102 ± 0.002	-0.064 ± 0.005	0.103 ± 0.005	6/11
		3.32	$ y < 0.25$	32.4 ± 2.2	0.115 ± 0.002	-0.057 ± 0.005	0.109 ± 0.005	1/7
		3.84		31.8 ± 2.1	0.140 ± 0.002	-0.048 ± 0.005	0.113 ± 0.005	1/6
		4.30		31.0 ± 2.0	0.149 ± 0.002	-0.039 ± 0.005	0.116 ± 0.005	1/4
		4.88		30.3 ± 2.0	0.151 ± 0.002	-0.036 ± 0.005	0.119 ± 0.005	1/6
Figure 10(e)	p	2.70	0–5%	22.0 ± 1.1	0.106 ± 0.002	-0.016 ± 0.004	0.324 ± 0.005	8/34
		3.32	$ y < 0.05$	21.3 ± 1.1	0.114 ± 0.002	-0.013 ± 0.004	0.330 ± 0.005	14/35
		3.84		20.5 ± 1.0	0.116 ± 0.002	-0.010 ± 0.004	0.334 ± 0.005	9/35
		4.30		19.6 ± 0.9	0.122 ± 0.002	-0.003 ± 0.004	0.342 ± 0.005	9/35

C. Further discussions

We now discuss this topic further. As we know, high energy collisions contain abundant information which are related to the productions of QGP and particles [55–62]. Of course, after a very short time, QGP finally decays into particles. The final-state products are naturally various kinds of particles. Indeed, understanding the characteristics of particle productions is particularly necessary for researchers to study the evolution of collision system and interactions among various particles [63–70]. By studying the particle spectra, this paper has extracted some quantities.

From the above comparison, one can see that this paper has used the transverse mass which contains the average transverse flow velocity $\langle\beta_t\rangle$ through the Lorentz-like transformation, $m'_T \rightarrow \langle\gamma_t\rangle(m_T - p_T\langle\beta_t\rangle)$ [49]. Considering the influence of transverse flow, the effective temperature T in Eq. (1) has been changed to the thermal freeze-out temperature T_0 in Eq. (2). In this way, T_0 and $\langle\beta_t\rangle$ can be directly extracted [49]. In this work, T_0 and $\langle\beta_t\rangle$ are quantities at the quark level, but not the quantities at the particle level. This renders that the values

obtained at the two levels are different.

There is a relation between the power index n and the entropy index q , $n = 1/(q - 1)$. It shows indeed that a larger n corresponds to a smaller q that is also closer to 1. As we know, an exact and concrete q that separates an approximate equilibrium and non-equilibrium states is not available in literature. Empirically, we may use $q = 1.25$, i.e. $n > 4$, as the boundary between the approximate equilibrium and non-equilibrium states. The present work shows that $n > 4$ in most cases. This means that the system in terms of quarks or partons discussed here is at the approximate equilibrium or local equilibriums. The concept of temperature can be approximately used.

At lower energy and in central collisions, the system consisted of quarks or partons is at larger degree of equilibrium. This is understood in view of the longer reaction time in lower collision energy and more participant partons in central collisions. These two factors can affect the system to be at more equilibrium due to more cascade collisions happening. At the present energy at the LHC, the system is approximately at the equilibrium. It is possible that at very high energy the system will be

at non-equilibrium due to very short reaction time. In most cases, the system in peripheral collisions is approximately at the equilibrium. It is not preclusive that in very peripheral collisions the system is possible at non-equilibrium due to very less cascade collisions in very limited collision volume, where the multiplicity is also low.

There are possible scenarios for single, double, or multiple kinetic freeze-out in literature. The single (two or multiple) kinetic freeze-out means that a set (two or multiple sets) of parameters can fit the spectra. There is not a solid conclusion for a definite scenario. The present work shows that some parameters from different particle spectra are different. This reflects the scenario for multiple kinetic freeze-out in high-energy collisions. According to the present work, we may say that different particles are produced in the system at different times. The decay of the system is not all at once, but successive.

The value of T_0 reflects the excitation degree of the system at the parton level, which is somehow larger than that at the particle level, due to the former happening earlier. The higher the value of T_0 is, the higher the excitation degree of the system is, and the larger the deposited energy is. The value of $\langle\beta_t\rangle$ reflects impact and squeeze between the projectile and target at parton level. In high energy collisions, a lot of energy are deposited in the process of parton interactions, though some partons go through the system as spectators.

Some soft excitation and hard scattering processes among partons have happened. The contribution of soft component from resonance in π^\mp spectra is significantly larger than those in K^\mp and $\bar{p}(p)$ spectra. This renders that the spectra of π^\mp have a significant increase in low- p_T region, comparing with the spectra of other particles. This change in low- p_T region is mainly described by the value of a_0 in this work. A small a_0 describes a significant increase and a large a_0 describes a decrease. Naturally, this change also affects the parameters n , T_0 , and $\langle\beta_t\rangle$.

Indeed, for π^\mp spectra in low- p_T region, the production of resonances cannot be ignored. More contributions from the resonances in π^\mp productions render that the shape of the spectra of the considered different kinds of particles are different, in particular in low- p_T region. This also renders the different sets of parameters for different particles. In addition, multiple kinetic freeze-out also results in multiple sets of parameters. The earlier

the particles are emitted, the wider the spectrum is, and the higher the temperature is.

At given collision energy, the nuclear environments (the sizes of participant or spectator regions) in central and peripheral Au-Au collisions have some influences on the transverse momentum spectra. We attribute this phenomenon to the hadronic cascade collisions (or multiple scattering) in hot and dense participant zone. The larger number of participants in central collisions means more cascade collisions and, hence, the larger transverse momentum and temperature. In the considered transverse momentum region, the changing laws of transverse momentum spectra for given particles are independent of isospin. Compared with strong interactions, contribution of electromagnetic interactions is very small and negligible.

The purpose of the RHIC-BES program is to search for the critical point in the QCD phase diagram. In the RHIC-BES and the related AGS energy regions, from the energy dependences of related parameters in the available central collisions, we found that T_0 and S'_{hadron} increase quickly and then slowly at around 7.7 GeV with the increase of collision energy. This special energy is the knee point of the equation of state (EoS) of the hot and dense matter, which is related to the critical energy, if not equal. Meanwhile, we found that a_0 increases and then decreases at around 7.7 GeV in the available central collisions. Generally, different parameters may reveal different knee points. The most probable knee point from the energy dependences of various parameters can be regarded as the critical point.

In the available central collisions, both the boundary energies of the rapid-slow increase in the energy dependence of T_0 and S'_{hadron} and of the increase-decrease change in the energy dependence of a_0 are 7.7 GeV. We argue that this energy is possibly the critical energy of deconfinement phase transition from hadronic matter to QGP. Because of the complexity of the collision process, the conclusion about the critical energy in this work is not solid. A shift of 2–3 GeV is possible. To make a solid conclusion, one needs a comprehensive analysis of various parameters. At least, we may state that the interaction mechanisms or strengths at the energy below and above about 7.7 GeV are different.

IV. SUMMARY AND CONCLUSIONS

In this paper, the TP-like function has been used to analyze the transverse momentum spectra of the charged particles [π^\mp , K^\mp , and $\bar{p}(p)$] produced in Au-Au collisions at the RHIC-BES energies and the related AGS energies. The contribution of each constituent quark to the transverse momentum of charged particle is assumed to satisfy the TP-like function. Each constituent quark is also regarded as an energy resource. Therefore, the transverse momentum spectrum of mesons (baryons) is the convolution of two (three) TP-like functions. According to the fitting results, we have obtained four parameters: the power index n , the thermal freeze-out temperature T_0 , the correction index a_0 , and the average transverse flow velocity $\langle\beta_t\rangle$. The dependences of these parameters on collision energy and centrality have been also investigated.

It is obvious that with the increase of collision energy, n decreases, which indicates that the collision system is farther away from the equilibrium, though it is still approximately at the equilibrium, at higher energy. In other words, at lower energy, the longer the collision evolves, the closer to the equilibrium the system is. More importantly, with the increase of collision energy, T_0 extracted from meson spectra in central Au-Au collisions increases quickly in the range of less than 7.7 GeV and slowly in the range of greater than 7.7 GeV. Meanwhile, $\langle\beta_t\rangle$ increases with the increase of collision energy. From central to peripheral collisions, all of n , T_0 , and $\langle\beta_t\rangle$ decrease, and a_0 increases. Even in peripheral collisions, the system is approximately at the equilibrium.

We have introduced the concept and definition of a new quantity, the pseudo-entropy. The pseudo-entropy is carried out a more in-depth study on the transverse momentum spectra of charged particles. With the increase of collision energy, the pseudo-entropy extracted from the meson spectra in central Au-Au collisions increases quickly in the range of less than 7.7 GeV and slowly in the range of greater than 7.7 GeV. This behavior is similar to that for T_0 . We argue that 7.7 GeV is a special energy at which the phase transition of deconfinement from hadronic matter to QGP can possibly happen. At least, the interaction mechanism in the system or the production mechanism of charged

particles at the energy below and above about 7.7 GeV are different.

Data Availability

The data used to support the findings of this study are included within the article and are cited at relevant places within the text as references.

Ethical Approval

The authors declare that they are in compliance with ethical standards regarding the content of this paper.

Disclosure

The funding agencies have no role in the design of the study; in the collection, analysis, or interpretation of the data; in the writing of the manuscript; or in the decision to publish the results.

Conflicts of Interest

The authors declare that there are no conflicts of interest regarding the publication of this paper.

Acknowledgments

The work of X.H.Z. and F.H.L. was supported by the National Natural Science Foundation of China under Grant Nos. 12147215, 12047571, 11575103, and 11947418, the Scientific and Technological Innovation Programs of Higher Education Institutions in Shanxi (STIP) under Grant No. 201802017, the Shanxi Provincial Natural Science Foundation under Grant No. 201901D111043, and the Fund for Shanxi “1331 Project” Key Subjects Construction. The work of X.H.Z. was also supported by the Innovative Foundation for Graduate Education in Shanxi University. The work of Y.Q.G. was supported by the Scientific and Technological Innovation Programs of Higher Education Institutions in Shanxi (STIP) under Grant No. 2019L0629. The work of K.K.O. was supported by the Ministry of Innovative Development of the Republic of Uzbekistan within the fundamental project No. F3-20200929146 on analysis of open data on heavy-ion collisions at RHIC and LHC.

-
- [1] S. Badger, J. M. Campbell, and R. K. Ellis, “QCD corrections to the hadronic production of a heavy quark pair and a W -boson including decay correlations,” *Journal of High Energy Physics*, vol. 2011, no. 3, article 27, 2011.
- [2] J. Gao, C. S. Li, B. H. Li, H. X. Zhu, and C.-P. Yuan, “Next-to-leading order QCD corrections to a heavy resonance production and decay into top quark pair at the LHC,” *Physical Review D*, vol. 82, no. 1, article 014020, 2010.
- [3] D. J. Gross, “The discovery of asymptotic freedom and the emergence of QCD,” *International Journal of Modern Physics A*, vol. 20, no. 25, pp. 5717–5740, 2005; D. J. Gross, “The discovery of asymptotic freedom and the emergence of QCD,” *Proceedings of the National Academy of Sciences of the United States of America*, vol. 102, no. 26, pp. 9099–9108, 2005; D. J. Gross, “Nobel Lecture: The discovery of asymptotic freedom and the emergence of QCD,” *Review of Modern Physics*, vol. 77, no. 3, pp. 837–849, 2005.
- [4] A. Khuntia, S. Tripathy, R. Sahoo, and J. Cleymans, “Multiplicity dependence of non-extensive parameters for strange and multi-strange particles in proton-proton collisions at $\sqrt{s} = 7$ TeV at the LHC,” *The European Physical Journal A*, vol. 53, no. 5, article 103, 2017.
- [5] H. Satz and R. Stock, “Quark matter: The beginning,” *Nuclear Physics A*, vol. 956, pp. 898–901, 2016.
- [6] S. Furusawa, T. Sanada, and S. Yamada, “Hydrodynamical study on the conversion of hadronic matter to quark matter: II. diffusion-induced conversion,” *Physical Review D*, vol. 93, no. 4, article 043019, 2016.
- [7] S. Imai, H. Toki, and W. Weise, “Quark-hadron matter at finite temperature and density in a two-color PNJL model,” *Nuclear Physics A*, vol. 913, pp. 71–102, 2013.
- [8] B. Liu, M. D. Toro, G. Y. Shao, V. Greco, C. W. Shen, and Z. H. Li, “Hadron-quark phase coexistence in a hybrid MIT-Bag model,” *The European Physical Journal A*, vol. 47, no. 9, article 104, 2011.
- [9] B. Mohanty, “Exploring the quantum chromodynamics landscape with high-energy nuclear collisions,” *New Journal of Physics*, vol. 13, no. 6, article 065031, 2011.
- [10] P. Braun-Munzinger and J. Wambach, “Colloquium: Phase diagram of strongly interacting matter,” *Reviews of Modern Physics*, vol. 81, no. 3, pp. 1031–1050, 2009.
- [11] K. Fukushima and T. Hatsuda, “The phase diagram of dense QCD,” *Reports on Progress in Physics*, vol. 74, no. 1, article 014001, 2011.
- [12] N. Bratovic, T. Hatsuda, and W. Weise, “Role of vector interaction and axial anomaly in the PNJL modeling of the QCD phase diagram,” *Physics Letters B*, vol. 719, nos. 1–3, pp. 131–135, 2013.
- [13] S. Carignano, D. Nickel, and M. Buballa, “Influence of vector interaction and Polyakov loop dynamics on inhomogeneous chiral symmetry breaking phases,” *Physical Review D*, vol. 82, no. 5, article 054009, 2010.
- [14] L. Adamczyk, J. K. Adkins, G. Agakishiev et al. (STAR Collaboration), “Collision energy dependence of moments of net-kaon multiplicity distributions at RHIC,” *Physics Letters B*, vol. 785, pp. 551–560, 2018.
- [15] L. Adamczyk, J. K. Adkins, G. Agakishiev et al. (STAR Collaboration), “Energy dependence of moments of net-proton multiplicity distributions at RHIC,” *Physical Review Letters*, vol. 112, no. 3, article 032302, 2014.
- [16] L. Adamczyk, J. K. Adkins, G. Agakishiev et al. (STAR Collaboration), “Beam-energy dependence of the directed flow of protons, antiprotons, and pions in Au+Au collisions,” *Physical Review Letters*, vol. 112, no. 16, article 162301, 2014.
- [17] L. Adamczyk, J. K. Adkins, G. Agakishiev et al. (STAR Collaboration), “Beam energy dependence of moments of the net-charge multiplicity distributions in Au+Au collisions at RHIC,” *Physical Review Letters*, vol. 113, no. 9, article 092301, 2014.
- [18] X. F. Luo, “Exploring the QCD phase structure with beam energy scan in heavy-ion collisions,” *Nuclear Physics A*, vol. 956, pp. 75–82, 2016.
- [19] S. Ejiri, R. Iwami, and N. Yamada, “Critical point search from an extended parameter space of lattice QCD at finite temperature and density,” *Nuclear Physics A*, vol. 956, pp. 826–829, 2016.
- [20] I. Arsene, I. G. Bearden, D. Beavis et al. (BRAHMS Collaboration), “Quark-gluon plasma and color glass condensate at RHIC? The perspective from the BRAHMS experiment,” *Nuclear Physics A*, vol. 757, nos. 1–2, pp. 1–27, 2005.
- [21] K. Adcox, S. S. Adler, S. Afanasiev et al. (PHENIX Collaboration), “Formation of dense partonic matter in relativistic nucleus-nucleus collisions at RHIC: Experimental evaluation by the PHENIX Collaboration,” *Nuclear Physics A*, vol. 757, nos. 1–2, pp. 184–283, 2005.
- [22] B. B. Back, M. D. Baker, M. Ballintijn et al. (PHOBOS Collaboration), “The PHOBOS perspective on discoveries at RHIC,” *Nuclear Physics A*, vol. 757, nos. 1–2, pp. 28–101, 2005.

- [23] J. Adams, M. M. Aggarwal, Z. Ahammed et al. (STAR Collaboration), “Experimental and theoretical challenges in the search for the quark-gluon plasma: The STAR Collaboration’s critical assessment of the evidence from RHIC collisions,” *Nuclear Physics A*, vol. 757, nos. 1–2, pp. 102–183, 2005.
- [24] L. Kumar for the STAR Collaboration, “Bulk properties in Au+Au collisions at $\sqrt{s_{NN}} = 9.2$ GeV in STAR experiment at RHIC,” *Nuclear Physics A*, vol. 830, nos. 1–4, pp. 275c–278c, 2009.
- [25] B. Mohanty, “QCD phase diagram: Phase transition, critical point and fluctuations,” *Nuclear Physics A*, vol. 830, nos. 1–4, pp. 899c–907c, 2009.
- [26] C. Yang for the STAR Collaboration, “The STAR detector upgrades and physics in beam energy scan phase II,” *EPJ Web of Conferences*, vol. 182, article 02130, 2018.
- [27] K. C. Meehan for the STAR Collaboration, “Fixed target collisions at STAR,” *Nuclear Physics A*, vol. 956, pp. 878–881, 2016.
- [28] X. Sun for the STAR Collaboration, “Flow in the RHIC beam energy scan from STAR,” *Journal of Physics: Conference Series*, vol. 535, article 012005, 2014.
- [29] K. C. Meehan for the STAR Collaboration, “The fixed-target experiment at STAR,” *Journal of Physics: Conference Series*, vol. 742, article 012022, 2016.
- [30] G. Odyniec, “The RHIC beam energy scan program in STAR and what’s next ...,” *Journal of Physics: Conference Series*, vol. 455, article 012037, 2013.
- [31] J. Cleymans, H. Oeschler, K. Redlich, and S. Wheaton, “Comparison of chemical freeze-out criteria in heavy-ion collisions,” *Physical Review C*, vol. 73, no. 3, article 034905, 2006.
- [32] C. Yang for the STAR Collaboration, “The STAR beam energy scan phase II physics and upgrades,” *Nuclear Physics A*, vol. 967, pp. 800–803, 2017.
- [33] L. Adamczyk, J. K. Adkins, G. Agakishiev et al. (STAR Collaboration), “Bulk properties of the medium produced in relativistic heavy-ion collisions from the beam energy scan program,” *Physical Review C*, vol. 96, no. 4, article 044904, 2017.
- [34] J. Adam, L. Adamczyk, J. R. Adams et al. (STAR Collaboration), “Bulk properties of the system formed in Au+Au collisions at $\sqrt{s_{NN}} = 14.5$ GeV at the BNL STAR detector,” *Physical Review C*, vol. 101, no. 2, article 024905, 2020.
- [35] B. I. Abelev, M. M. Aggarwal, Z. Ahammed et al. (STAR Collaboration), “Systematic measurements of identified particle spectra in pp , $d+Au$, and Au+Au collisions at the STAR detector,” *Physical Review C*, vol. 79, no. 3, article 034909, 2009.
- [36] J. L. Klay, N. N. Ajitanand, J. M. Alexander et al. (E895 Collaboration), “Charged pion production in $2A$ to $8A$ GeV central Au+Au collisions,” *Physical Review C*, vol. 68, no. 5, article 054905, 2003.
- [37] L. Ahle, Y. Akiba, K. Ashktorab et al. (E866 and E917 Collaborations), “An excitation function of K^- and K^+ production in Au+Au reactions at the AGS,” *Physics Letters B*, vol. 490, no. 1, pp. 53–60, 2000.
- [38] J. L. Klay, N. N. Ajitanand, J. M. Alexander et al. (E895 Collaboration), “Longitudinal flow of protons from $(2-8)A$ GeV central Au+Au Collisions,” *Physical Review Letters*, vol. 88, no. 10, article 102301, 2002.
- [39] C. Tsallis, “Possible generalization of Boltzmann-Gibbs statistics,” *Journal of Statistical Physics*, vol. 52, nos. 1–2, pp. 479–487, 1988.
- [40] T. S. Biró, G. Purcsel, and K. Ürmössy, “Non-extensive approach to quark matter,” *The European Physical Journal A*, vol. 40, no. 3, pp. 325–340, 2009.
- [41] H. Zheng and L. L. Zhu, “Can Tsallis distribution fit all the particle spectra produced at RHIC and LHC?,” *Advances in High Energy Physics*, vol. 2015, article 180491, 2015.
- [42] H. Zheng, L. L. Zhu, and A. Bonasera, “Systematic analysis of hadron spectra in $p+p$ collisions using Tsallis distributions,” *Physical Review D*, vol. 92, no. 7, article 074009, 2015.
- [43] S. Charchyan, V. Khachatryan, A. M. Sirunyan et al. (CMS Collaboration), “Study of the inclusive production of charged pions, kaons, and protons in pp collisions at $\sqrt{s} = 0.9, 2.76, \text{ and } 7$ TeV,” *The European Physical Journal C*, vol. 72, no. 10, article 2164, 2012.
- [44] J. Cleymans and M. W. Paradzka, “Tsallis statistics in high energy physics: Chemical and thermal freeze-outs,” *Physics*, vol. 2, no. 4, pp. 654–664, 2020.
- [45] P.-P. Yang, F.-H. Liu, and R. Sahoo, “A new description of transverse momentum spectra of identified particles produced in proton-proton collisions at high energies,” *Advances in High Energy Physics*, vol. 2020, article 6742578, 2020.
- [46] Y.-M. Tai, P.-P. Yang, and F.-H. Liu, “An analysis of transverse momentum spectra of various jets produced in high energy collisions,” *Advances in High Energy Physics*, vol. 2021, article 8832892, 2021.
- [47] E. Schnedermann, J. Sollfrank, and U. Heinz, “Thermal phenomenology of hadrons from $200A$ GeV S+S collisions,” *Physical Review C*, vol. 48, no. 5, pp. 2462–2475, 1993.

- [48] M. Waqas and B.-C. Li, “Kinetic freeze-out temperature and transverse flow velocity in Au-Au collisions at RHIC-BES energies,” *Advances in High Energy Physics*, vol. 2020, article 1787183, 2020.
- [49] P. K. Khandai, P. Sett, P. Shukla, and V. Singh, “System size dependence of hadron p_T spectra in $p+p$ and Au+Au collisions at $\sqrt{s_{NN}} = 200$ GeV,” *Journal of Physics G*, vol. 41, no. 2, article 025105, 2014.
- [50] Z.-J. Xiao and C.-D. Lü, Introduction to Particle Physics, Science Press, Beijing, China, p. 160, March 2016
- [51] V. Andreev, A. Baghdasaryan, A. Baty et al. (H1 Collaboration), “Measurement of charged particle multiplicity distributions in DIS at HERA and its implication to entanglement entropy of partons,” *The European Physical Journal C*, vol. 81, no. 3, article 212, 2021.
- [52] X. Feal, C. Pajares, and R. A. Vazquez, “Thermal behavior and entanglement in Pb-Pb and $p-p$ collisions,” *Physical Review C*, vol. 99, no. 1, article 015205, 2019.
- [53] Z. Tu, D. E. Kharzeev, and T. Ullrich, “Einstein-Podolsky-Rosen paradox and quantum entanglement at subnucleonic scales,” *Physical Review Letters*, vol. 124, no. 6, article 062001, 2020.
- [54] D. E. Kharzeev and E. M. Levin, “Deep inelastic scattering as a probe of entanglement,” *Physical Review D*, vol. 95, no. 11, article 114008, 2017.
- [55] A. Motornenko, V. Vovchenko, C. Greiner, and H. Stoecker, “Kinetic freeze-out temperature from yields of short-lived resonances,” *Physical Review C*, vol. 102, no. 2, article 024909, 2020.
- [56] J. A. L. López on behalf of the ATLAS Collaboration, “Measurement of charmonium production in heavy-ion collisions with the ATLAS detector,” *Nuclear Physics A*, vol. 967, pp. 584-587, 2017.
- [57] G. R. Che, J. B. Gu, W. C. Zhang, and H. Zheng, “Identified particle spectra in Pb-Pb, Xe-Xe and p-Pb collisions with the Tsallis blast-wave model,” *Journal of Physics G*, vol. 48, no. 9, article 095103, 2021.
- [58] A. Jaiswal, N. Haque, A. Abhishek et al., “Dynamics of QCD matter – current status,” *International Journal of Modern Physics E*, vol. 30, no. 2, article 2130001, 2021.
- [59] J. Chen, J. Deng, Z. B. Tang, Z. B. Xu, and L. Yi, “Nonequilibrium kinetic freeze-out properties in relativistic heavy ion collisions from energies employed at the RHIC beam energy scan to those available at the LHC,” *Physical Review C*, vol. 104, no. 3, article, 034901, 2021.
- [60] X. F. Luo, S. S. Shi, N. Xu, and Y. F. Zhang, “A study of properties of the QCD phase diagram in high-energy nuclear collisions,” *Particles*, vol. 3, no. 2, pp. 278-307, 2020.
- [61] S. Bhattacharyya, “Backward shower particle production in high energy nucleus-nucleus collisions – an outlook to centrality dependence,” *International Journal of Modern Physics E*, vol. 30, no. 4, article 2150032, 2021.
- [62] S. Chatterjee, S. Das, L. Kumar, D. Mishra, B. Mohanty, R. Sahoo, and N. Sharma, “Freeze-out parameters in heavy-ion collisions at AGS, SPS, RHIC, and LHC energies,” *Advances in High Energy Physics*, vol. 2015, article 349013, 2015.
- [63] A. Bacchetta, F. Delcarro, C. Pisano, M. Radici, and A. Signori, “Extraction of partonic transverse momentum distributions from semi-inclusive deep-inelastic scattering, Drell-Yan and Z-boson production,” *Journal of High Energy Physics*, vol. 2017, no. 6, article 081, 2017.
- [64] V. V. Anisovich, S. M. Gerasyuta and A.V. Sarantsev, “Low-lying meson spectroscopy and confinement,” *International Journal of Modern Physics A*, vol. 6, no. 4, pp. 625-666, 1991.
- [65] L. Adamczyk, J. K. Adkins, G. Agakishiev et al. (STAR Collaboration), “Global Λ hyperon polarization in nuclear collisions” *Nature*, vol. 548, pp. 62-65, 2017.
- [66] S. A. Bass, M. Gyulassy, H. Stöcker, and W. Greiner, “Signatures of quark-gluon plasma formation in high energy heavy-ion collisions: a critical review,” *Journal of Physics G*, vol. 25, no. 3, pp. R1-R57, 1999.
- [67] D. Stauffer, “Scaling theory of percolation clusters,” *Physics Reports*, vol. 54, no. 1, pp. 1-74, 1979.
- [68] W. Busza, K. Rajagopal, and W. van der Schee, “Heavy ion collisions: The big picture and the big questions,” *Annual Review of Nuclear and Particle Science*, vol. 68, pp. 339-376, 2018.
- [69] W.-J. Xie, and F.-S. Zhang, “Nuclear collective flows as a probe to the neutron-proton effective mass splitting,” *Physics Letters B*, vol. 735, no. 30, pp. 250-255, 2014.
- [70] D. E. Kharzeev, J. Liao, S. A. Voloshin, and G. Wang, “Chiral magnetic and vortical effects in high-energy nuclear collisions – A status report,” *Progress in Particle and Nuclear Physics*, vol. 88, pp. 1-28, 2016.